

Study of the Photon Transfer Curve in the CCD detectors of the Vera C. Rubin Observatory

Lina Marcela Giraldo-Murillo^{a*}

Advisors: Andrés A. Plazas Malagón^b & Craig Lage^c

^aInstituto de Física, Universidad de Antioquia, Medellín, Colombia

^b SLAC National Accelerator Laboratory, 2575 Sand Hill Rd, Menlo Park, CA, 94025, USA

Kavli Institute for Particle Astrophysics & Cosmology, P.O. Box 2450, Stanford University, Stanford, California 94305, USA

Department of Astrophysical Sciences, Peyton Hall, Princeton University, Princeton, NJ 08544, USA

^cDepartment of Physics, University of California, Davis, USA

* lina.giraldom@udea.edu.co

November 2, 2022

Abstract

The RECA internship program allows Colombian students to get better research skills in Astronomy, Astrophysics, and Cosmology. For three months, we developed our work in this internship program, and its main objective was to study the photon transfer curves (PTC) of the Vera C. Rubin Observatory, mainly gain, and to make comparisons with the gain obtained through pairs of flats.

We used run 13144 to construct the PTCs and 13186 to analyze the crosstalk. We use *DM stack*, which is the software in development for this observatory, and it makes all the reductions for the construction of the PTCs. Also, we implement simulations to reproduce the observed effects.

We initially found a 5 % difference between the gain by PTC and pairs of flats in a range of flows between 5000 and 10000 ADU. Simulations showed that this difference was a product of the handling of the statistics and the erroneous assumption that the distribution following the Lupton equation is Gaussian. By vendor, we found an error interval for this flow region, for E2V of $(1.8 \pm 0.7, 4.1 \pm 0.9)$ % and for ITL of $(0.85 \pm 0.7, 2.2 \pm 0.9)$ %. Also, from the PTC we found the average Full Well Capacity of LSSTCam is 130000 ± 10000 e⁻.

We obtained a list of segments where we found differences with the results obtained by SLAC National Acceleration Laboratory in PTC parameters, low saturation level, or other defects. We detected and corrected the effect of statistics in the gain calculation using pairs of flats. Then, we proposed a code change for it, which was implemented in *DM stack*. In addition, we do not recommend correcting for crosstalk since it does not significantly affect the parameters and does not change the shape of the PTC; the opposite is true for the nonlinearity correction.

Keywords— PTC; Gain; Crosstalk; Linearity, Brighter Fatter effect, Full Well Capacity

1 Introduction

The Vera C. Rubin Observatory is located at Cerro Pachón in the Atacama Desert in Chile. It was chosen after considering different sites worldwide according to their meteorological conditions. It will operate the

8.4-meter Simonyi Research Telescope, which will be able to scan the entire southern sky in approximately three nights and is expected to start operations in 2024. This observatory also has the giant camera ever built, the LSST Camera, which has a 3.2 gigapixel resolution for the entire focal plane, with a diameter of 64 cm to cover 9.6 deg² FoV and a plate scale of 0.2 " pixel⁻¹ (LSST Science Collaboration et al., 2009).

This observatory is named in honor of the astronomer Vera Rubin (NSF, 2020), who in 1970 pioneered the measurement of the rotation curves of disk galaxies (Rubin, 2011), in which she realized that for the stars in galaxies to rotate at the rate they do, there must be more mass than we observe for the galaxies not to break apart. This mass is what we now call dark matter, which is one of the scientific goals of this observatory.

Vera Rubin received several awards, including the National Medal of Science, and even a ridge on Mars is named after her (Koren, 2020). In addition, she worked hard for the recognition of the work of women in science and her students (Rubin, 2011).

1.1 LSST Scientific goals

The LSST has four main scientific objectives (Ivezić et al., 2019; LSST Science Collaboration et al., 2009):

- Taking an Inventory of the Solar System: The minor bodies of the solar system, such as TNOs, asteroids, and comets, are crucial to understanding planetary formation and evolution since their orbital elements and sizes preserve this history. On the other hand, the interaction of objects in the Main Asteroid Belt, which lies between Mars and Jupiter, could launch some of these objects into Earth's orbit, so their study will help to make a connection between NEOs coming from the Main Belt.
- Mapping the Milky Way: It concerns the study of the formation and evolution of our galaxy by observing its stars' structure, dynamics, and chemical composition. In addition, this science objective will characterize the stars in the solar neighborhood (300 pc).
- Exploring the Transient Optical Sky: This time domain science observes transient and variable phenomena such as supernovae, variable stars, and AGN. The goal is to detect transient and distant objects. This requires several properties: covering a large part of the sky to increase the probability of seeing these events, good quality images to observe the differences between images, good sampling time to detect the different types of variable stars, accurate color information for classification, long-term persistent observations to follow up the event, reduction, classification and rapid publication to the community to allow the study of these objects in other fields, such as spectroscopy.
- Probing Dark Energy and Dark Matter: Dark energy affects the universe's expansion as the accumulation of mass, so the observations must depend on the redshift to study it. For this purpose, they will study weak gravitational lensing, large-scale structures such as galaxy clusters, BAO (Baryonic AcoAcousticillation), and Supernova systems, among others. For the study of dark matter, there are several mechanisms to explore it, such as weak and strong lensing of galaxy mass distributions..

1.2 What kind of CCD does the LSST Camera have?

The LSSTCam is composed of *thick fully depleted* and back-illuminated CCDs(LSST Science Collaboration et al., 2009). This type of CCD is characterized by a good response in the near-infrared regions (Lage,

Bradshaw, & Tyson, 2017), which allows observation of distant objects reddened by the universe's expansion. However, being thick, they present some effects due to the long path that the generated electrons must travel to the charge storage well.

The LSSTCam is highly segmented, which enables it to be read out completely in 2 s and reduces the readout noise produced by high readout speeds (LSST Science Collaboration et al., 2009). It comprises a mosaic of 205 CCDs organized by 21 science modules, each containing nine CCDs and four specialized corner modules for telescope guidance and alignment by active optics (Snyder et al., 2020). This mosaic has CCDs from two vendors: Imaging Technology Laboratories (ITL) and Teledyne e2v (E2V), and each is divided into 16 segments. Figure 1 shows in yellow the vendor's E2V detectors, in greenish blue the ITL detectors, which are the science CCDs, and in purple the guidance CCDs.

According to Walter (2015) for the LSST science objective in weak lensing, where the aim is to measure how this modifies the shape of galaxies by observing a wide field, it is crucial to quantify the brighter-fatter (BF, hereafter) effect since exact measurements of the PSF of galaxies are required. The BF effect leads to the deformation of the PSF, being more critical in bright objects and progressively decreasing in fainter objects (Lage et al., 2017). On the other hand, Walter (2015) mentions that another effect suffered by the sensors is the edge effect, where electrons near the edge of the sensor feel a force that pushes them inward, which mainly affects astrometry.

1.3 What is Photon Transfer Curve (PTC)?

The Photon Transfer Curve (PTC) allows the characterization of the fundamental parameters of the CCD, mainly the determination of the relationship between the electrons recorded by each pixel and their conversion to analog-to-digital counts (ADU), i.e., the gain; it also measures the nonlinearity of the camera and its Full Well Capacity (FWC). The first parameter is essential because other vital parameters, such as read noise, quantum efficiency, dark current, among others, depend on it (Downing, Baade, Sinclair, Deiries, & Christen, 2006).

Figure 2 shows the PTC of segment C06 of sensor 22 of the LSSTCam, where it is evident that at low fluxes, the variance is low and increases with the flux but not linearly until the saturation point or FWC, which for this detector is 83000 ADU. After this point, the variance begins to decrease, indicating that the flux stored in each pixel of this amplifier begins to homogenize. The nonlinear behavior of this curve is exhibited by *thick fully-depleted CCDs*, according to Downing et al. (2006) charge storage in a pixel is the main reason, since the expected relationship between the variance and the mean number of counts in a pixel is modified in flat images (Walter, 2015). The effective area of the pixel changes with the amount of charge, decreasing the more significant the charge accumulated in the pixel. Consequently, very bright sources are mainly affected by this so-called BF effect. If the pixels of the CCD segment were independent, they could be described by Poisson statistics, and the PTC would follow the green line in the figure.

1.3.1 Brighter father effect

As mentioned above, the charge stored in a pixel modifies the effective area of the pixel, decreasing the probability that this pixel will continue to store the charge. Consequently, the electrons that should have been kept in this pixel are deflected horizontally, causing more elliptical images. Thus, a process initially described by a Poisson statistic, and the charge stored in each pixel was independent of the other, breaks down by modifying the relationship between the variance and the mean number of counts per pixel (Walter,

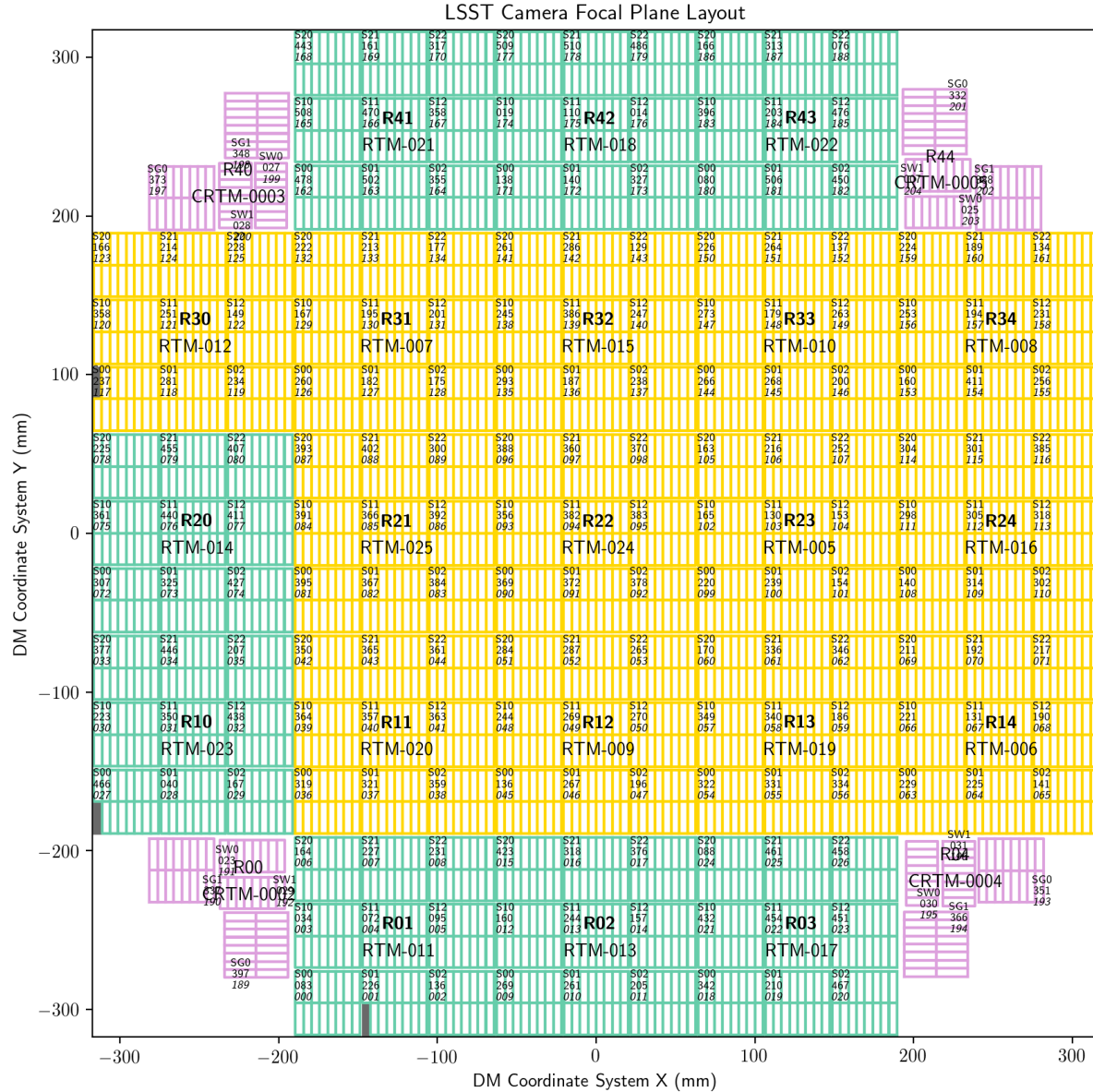


Figure 1: The focal plane of the LSST camera. The vendor's CCDs' location is blue for ITL and yellow for E2V. Each CCD (a small square) is composed of 16 segments, each with its amplifier, and 189 CCDs are responsible for taking the science data. The CCDs at the corners are for focusing and synchronization with the Earth's rotation (see LSST-SLACLab)

2015). This effect changes the PSF, so it is a potential problem in surveys interested in the variation of the brightness and shape of objects (Coulton, Armstrong, Smith, Lupton, & Spergel, 2018)

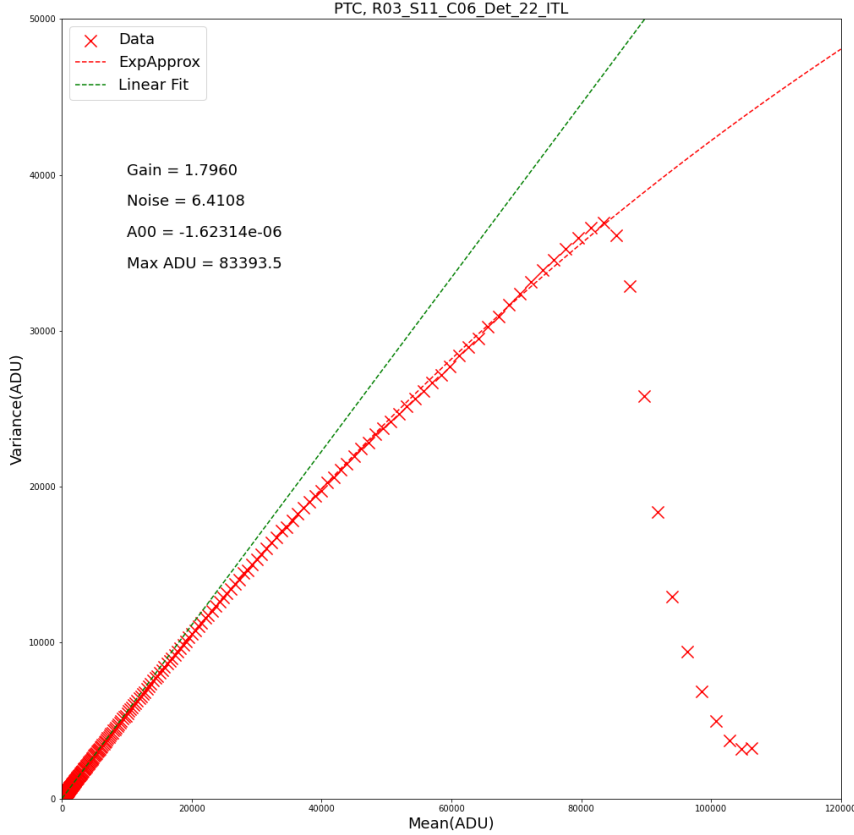


Figure 2: PTC for detector 22 was found in raft 03, sensor 11, and amplifier C06; its vendor is ITL. In red crosses, the data are shown, the red line uses the EXPAPPROXIMATION fit, and the green line is a linear fit. This curve was constructed with the results obtained via *DM stack*.

This work was developed during the RECA (Red de Estudiantes Colombiana de Astronomía) internship program 2022¹. The program was carried out over three months, in which we also developed other activities such as remote astronomical observations with the Teide Observatory².

In this report, we present the data used in the section 2. The section 3 describes the methodology used. In the section 4, we present the results and analysis. Finally, the conclusion in section 5.

2 Data

The data used in this work were obtained using the Bench for Optical Testing (BOT), which was built and designed at SLAC National Accelerator Laboratory. BOT allows laboratory tests with the LSSTCam with

¹RECA internship program is a training program in scientific research in Astronomy, Astrophysics, and Cosmology directed to students of Colombian institutions. The program website <https://recaastronomia.github.io/internship/>

²<https://www.iac.es/es/observatorios-de-canarias/observatorio-del-teide>

variations of less than 5 % in flat images so that measurements of the linearity, full well, and gain of the PTCs can be made (Newbry et al., 2018). Figure 3 shows the structure of the BOT, where the cryostat is located in the circular top and the focal plane is pointing down the test bench.

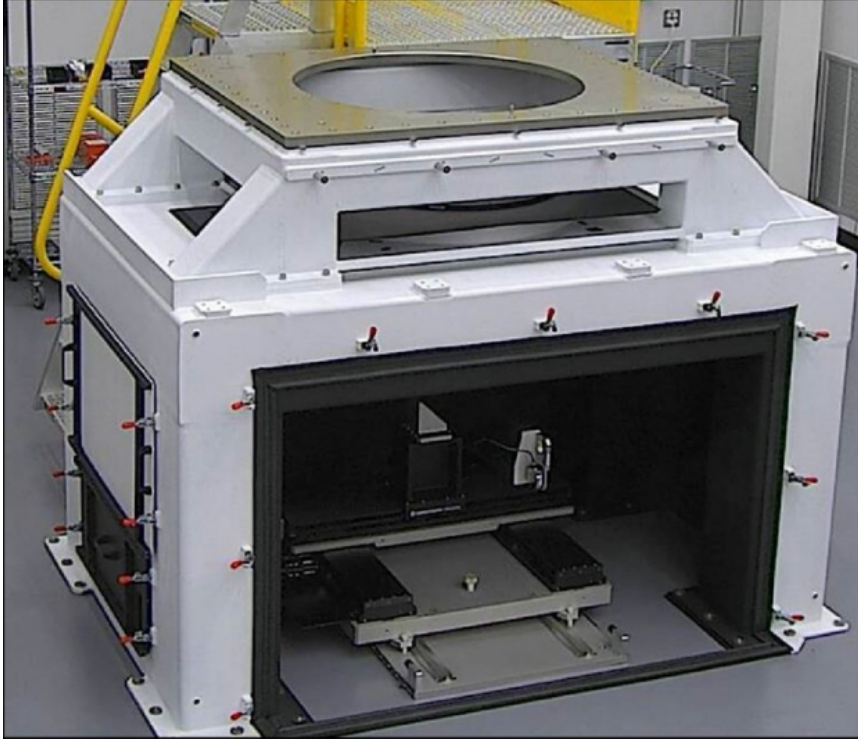


Figure 3: Bench for Optical Testing (BOT) designed by SLAC. Figure is taken from Newbry et al. (2018).

The *run 13144* and *run 13186* were used, the latter containing the crosstalk matrix information. According to Snyder et al. (2020), the electronic crosstalk measurements are carried out using a projector called *crosstalk projector*, which illuminates a single sensor with a pattern of large bright spots with a collimated beam of light, which has a radius of 80 pixels. However, to perform laboratory tests simulating real source sizes they used the optical projector called *the spot grid projector*. This projector generates spots in specific grids and has filters that simulate both lines left by satellites and the signal level of the sky background.

3 Methodology

The images used contain standard *overscan*, *bias*, *dark*, and *defects* reduction, which consist of maps indicating regions with both bright and dark defects, eg. dead pixels. The above reduction corresponds to the starting state for the PTC study. Subsequently, other corrections such as *linearity* and *crosstalk* are made to analyze their effects on the main parameters of the camera.

Professor Craig Lage generated supercalibrations for the entire focal plane, which are in a chain in his personal collection [u/cslage/calib/13144/calib.20220103](https://github.com/cslage/calib/13144/calib.20220103). Whereas, the images shown in Figures 4 and 5 are superbias and superdark (left panel E2V and right panel ITL), respectively, which were generated as part of the learning process for producing the calibration images using the software developed for the LSST, called *DM stack*.

The code with which the calibration images are generated via *DM stack* can be found in https://github.com/lsst/cp_pipe, and it generates the data for the construction of the PTC, calculates the gain for each CCD segment as its FWC. In addition, it calculates the gain by another different method, which was analyzed in section 3.2 to determine the differences between it and the PTC, which consists of using two pairs of flats for its estimation. We use two code versions of the *DM stack*³, for the entire focal plane:

- w_2022_27: Initial version we started working with.
- w_2022_32: Version that couples one of our main results on obtaining the gain with pairs of flats (see the DM-35790 ticket in Jira).

BPS (Batch Processing Service) was used to run the two previous versions. The details of how to build the configuration files, possible errors, associated link for more information, and how to use the obtained data can be found in the GitHub repository of this project RECA_Internship_Project in the notebook BPS_LSST.ipynb. In addition, all notebooks used to carry out the methodology described below are available in this repository. There is also a notebook called Tutorial.ipynb where I explain a little bit about the *Data Butler*, which is the API that manages and stores the data, where to find more information about it, what are the collections, visualize images, get the data and work with them, among other details about the calibration images.

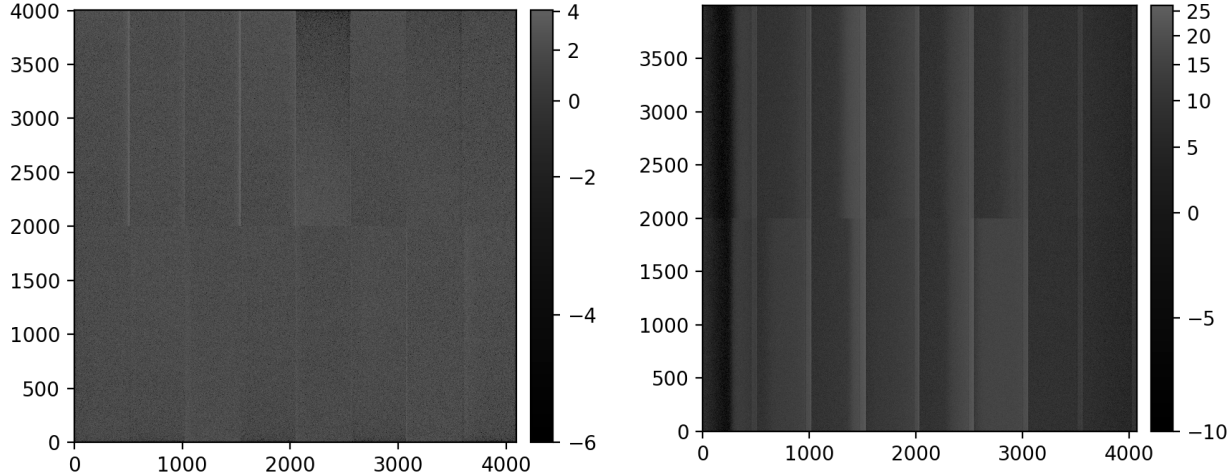


Figure 4: Masterbias for detectors 55 (E2V), on the left and 74 (ITL), on the right.

³DM stack is the software developed for the LSST and is publicly available on GitHub, and it can be found at <https://github.com/lsst/>

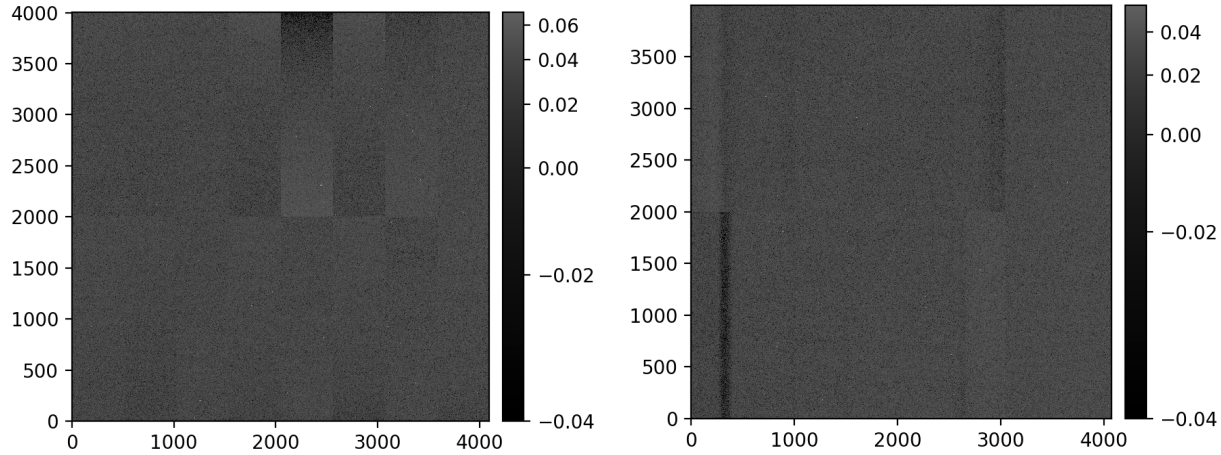


Figure 5: Masterdarks for detectors 55 (E2V), on the left and 74 (ITL), on the right.

3.1 Photon Transfer Curve (PTC)

The PTCs were generated for the whole LSSTCam focal plane using *DM stack*⁴, which allows estimating the gain, the read noise, a_{00} (parameter related to the B-F effect) and the turnoff (associated with the Full Well Capacity, FWC) from a fit to the shape of the PTC. This code implements equations 16 and 20 of the Astier et al. (2019) article: equation 16 corresponds to the exponential approximation (EXPAPPROXIMATION), which uses only the variance (C_{00}); while equation 20 is the full model (FULLCOVARIANCE), and implements the covariance matrix. In this work, we used EXPAPPROXIMATION, whose equation is as follows

$$C_{00} = \frac{1}{2g^2 a_{00}} [\exp(2a_{00}\mu g) - 1] + \frac{n_{00}}{g^2} \quad (1)$$

where C_{00} is the variance, g is the gain, a_{00} is always negative and is related to the B-F effect, μ is the mean, and n_{00} (e^l) is the noise. According to Astier et al. (2019), a_{00} being negative leads to the variance of a flat field not growing as fast as the mean does. In the case where there is no B-F effect, i.e., each pixel is independent of the other and is described by a Poisson statistic, the mean, gain, and variance are directly related through

$$V = \frac{\mu}{g} \quad (2)$$

where V is the variance of a flat field, μ is the mean, and g is the gain.

3.2 Gain from flat pairs

An independent method for calculating a sensor's gain is using flat field pairs with equal exposure times. Since each CCD is composed of 16 segments, each with its amplifier, a gain value is obtained for each

⁴The PTCs are constructed with the code available in the repository cp-pipe

segment. For this purpose, the LSST has the function Gain from flat pairs, which was analyzed in detail in this work.

We aim to quantify the difference between the gain calculated from the fit to the PTC and this method. For this, we initially calculate the average flux in ADU with each flat pair, the read noise, and the gain. The latter is estimated employing the equation of Lupton (2014)

$$\frac{1}{g} = \left\langle \frac{(I_1 - I_2)^2}{I_1 + I_2} \right\rangle \quad (3)$$

Where g is the gain, I_1 is the first flat image, and I_2 is the second flat image, both at the same exposure time. The expected value over all pixels is the inverse of gain. Considering the corrections for read-out noise, the equation takes the following quadratic form:

$$\frac{1}{g} = \left\langle \frac{(I_1 - I_2)^2}{I_1 + I_2} \right\rangle - \frac{1}{\mu} (N^2 - \frac{1}{2} g^2) \quad (4)$$

where $\mu u = 0.5(\mu_1 + \mu_2)$ with μu_1 and μu_2 the average value for each of the flat images and N is the read-out noise. This above equation has three variants: NONE, SIMPLE and FULL, with NONE being equal to the equation 3. The remaining two cases are as follows:

$$g = \begin{cases} \frac{1}{K - \frac{1}{\mu} (N^2 - \frac{1}{2} g^2)} & \text{SIMPLE} \\ \frac{\mu + \sqrt{\mu^2 - 2\mu K + 2N^2}}{2K\mu - 2K^2} & \text{FULL} \end{cases} \quad (5)$$

where K is equal to the equation 3. In the SIMPLE case $g = 1/K$, while in the FULL case the quadratic equation is solved and the result is taken to have physical meaning. Once we have the gains calculated from pairs of flats for flows between 0 and ~ 10000 ADU, we calculated the relative percentage error with the gain obtained with the fit to the PTC. We use the equation 5 with FULL type correction to calculate this relative error, thus:

$$\text{Relative_error}[\%] = \frac{|gain_{PTC} - gain_{flats}|}{gain_{PTC}} \times 100\% \quad (6)$$

Subsequently, a linear low-flow fit was performed, which we considered being between 5000 and 10000 ADU. The low-flow fit has the following form:

$$\text{Relative_error}_{LF}[\%] = mF + offset \quad (7)$$

where m is the slope of the fit, F is the flux, and $offset$ is the intercept with the y -axis. These parameters serve us to quantify the error variation in this flow range and the base error between the PTC gain and that calculated with the flats. We made histograms of these parameters to see the vendor's behavior and extract a general behavior. This is calculated by leaving out the outliers, i.e., the CCD segments with abnormal behavior. To do this, we made use of Astropy Collaboration et al. (2018) and its functions *sigma_clip* and *sigma_clipped_stats* with which we cut the data so that those that were within 3σ of the median were kept and we iterated three times.

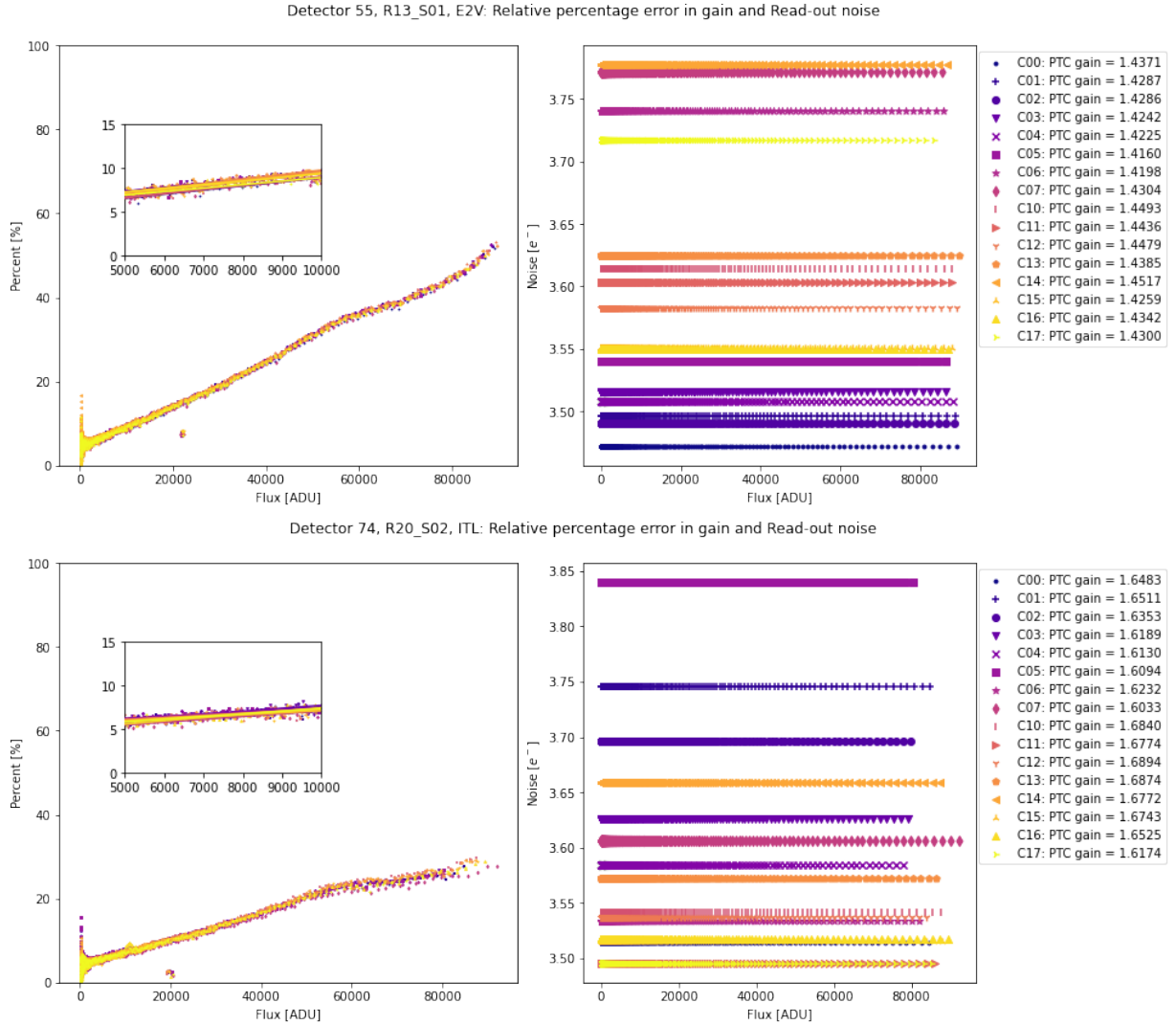


Figure 6: Relative percentage error between the gain estimated by the PTC and the gain calculated from two flat images (left), and the read-out noise of each amplifier (right), using the initial code. In the upper panel, it is shown for detector 55 (R13_S01), whose vendor is E2V, and in the lower panel for detector 74 (R20_S02) from the vendor ITL. Each color and symbol represents the relative percentage error for one of the 16 segments that make up each CCD. The embedded image in the left panels shows the percentage error between 5000 and 10000 ADU (low flux regime), in which a linear fit is made. The data used to construct these plots consider only those below the PTC turnoff.

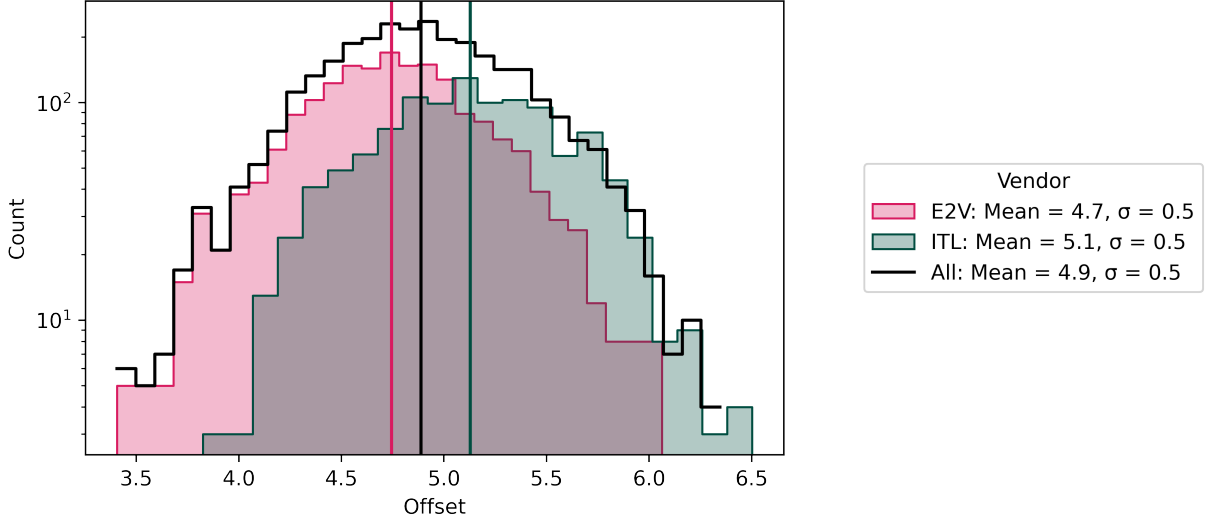


Figure 7: Histograms with the offset value obtained from the linear fit for flows between 5000 and 10000 ADU for the relative percentage error between gains. In magenta is shown the distribution for E2V, with a mean of (4.7 ± 0.5) %, and in blue for ITL, with a mean of (5.1 ± 0.5) %. The distribution in black represents the histogram of all data without discriminating by vendor, with a mean of (4.9 ± 0.5) %. The vertical lines represent the value of the mean for each of the distributions.

3.2.1 Simulation

The methodology described in section 3.2 and the use of the LSST software version *w_2022_27* led us to the results seen in Figures 6 and 7. Figure 6 shows the relative percent error between the gains over the flow range below the PTC turnoff for E2V sensor 55 (top panel) and ITL sensor 74 (bottom panel). The figure for each sensor has on the left an embedded plot showing the behavior between 5000 and 10000 ADU with its respective linear fit; on the right is the error of each of the CCD segments for the same flow range. We see in the embedded plot that the relative error has an offset higher than 5 % for these two sensors, so we made a histogram with the offset values for the entire focal plane and verified if this behavior is generalized. Figure 7 confirms that this relative error, on average, is a behavior exhibited by all sensors. We consider a base error of ~ 5 % to be relatively high, so we decided to investigate this problem through simulations.

Different variables could cause the problem described above to arise: an over-estimation of the readout noise, the mask used in the images is affecting, or another factor, such as the assumption that the distribution is Gaussian for the operation between the flat images given by

$$\frac{(I_1 - I_2)^2}{I_1 + I_2} \quad (8)$$

as it is being assumed in the *w_2022_27* version of the *DM stack*. If the distribution is not Gaussian, the distribution statistics are modified. We explored 3 cases through simulation to rule out or confirm variables, as described below:

- **Case 1 - Noise over-estimation:** Two data sets were constructed following a Poisson distribution for the flow, with an expected value between 5000 and 10000 ADU. In our case, we chose 5000 ADU. The distribution is then:

$$f(k; \lambda) = \frac{\lambda^k e^{-\lambda}}{k!} \implies f(k; 5000) = \frac{5000^k e^{-5000}}{k!} \quad (9)$$

where the expected value is λ , and k is the number of events. To the data following this distribution, we add a Gaussian noise whose mean is zero, and the value which gives the dispersion we will assume as the read-out noise, that is:

$$p(x) = \frac{1}{\sqrt{2\pi\sigma^2}} \exp\left(-\frac{(x-\mu)^2}{2\sigma^2}\right) \implies p(x) = \frac{1}{\sqrt{2\pi N^2}} \exp\left(-\frac{x^2}{2N^2}\right) \quad (10)$$

where the mean is μ , σ is the standard deviation, and N is the read-out noise, which we assume. Finally, we employ the methodology described in 3.2 for all types of gain correction: NONE, SIMPLE and FULL, and calculate the relative error using a base gain (we choose a value of 2.0) to verify if we can recreate what is observed in figure 6, i.e., a base error above 5 %.

- **Case 2 - Pixel masks:** As a next step, pixel masks are added to case 1. For this, the respective mask is extracted from each flat image, where each flat has an average of 5000 ADU counts. This mask filters out suspicious, bad, dead, and saturated pixels. A Poisson distribution is then generated with the dimensions of one of the CCD segments for which the masks were extracted, that is, $size_x = 2002$ and $size_y = 512$, with its respective Gaussian noise. The respective mask is applied to each array using the *Numpy* function (Harris et al., 2020) *ma.masked_where*.

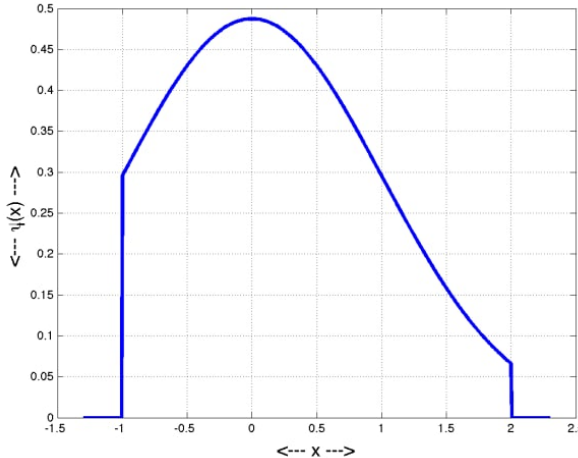


Figure 8: Truncated Gaussian distribution with both zero mean and standard deviation, $\psi(0, 1, a = -1, b = +2; x)$. Figure is taken from Burkardt (2014).

- **Case 3 - Statistics control:** To case 2, we add statistics control, i.e., we assume that the distribution of 8 is Gaussian, and we cut the distribution as it was done in the section 3.2, only in this case we keep all the data that are within 5.5σ of the mean, and we perform three iterations. Suppose the distribution of 8 is Gaussian. In that case, it must be satisfied that the mean of the truncated and original distribution is the same if symmetric cuts are made. When truncating non-symmetrically, the mean of this distribution is:

$$\mu = \bar{\mu} - \bar{\sigma} \frac{\phi(0, 1; \beta) - \phi(0, 1; \alpha)}{\Phi(0, 1; \beta) - \Phi(0, 1; \alpha)} ; \alpha = \frac{a - \bar{\mu}}{\bar{\sigma}}, \beta = \frac{b - \bar{\mu}}{\bar{\sigma}} \quad (11)$$

where α and β are standardized variables, a and b are the cutoff values for each side of the distribution, $\bar{\mu}$ and $\bar{\sigma}$ are the statistics of the original distribution, ϕ is the normal PDF, and Φ is the normal CDF. This case is illustrated in Figure 8 for $a = -1$ and $b = +2$. However, if $-a = b$, i.e., the distribution is symmetrically truncated, the numerator of the second term in the above equation becomes zero and is reduced to

$$\mu = \bar{\mu} \quad (12)$$

which implies that the mean of the truncated and the original distribution are equal. Therefore, we use this result to calculate the expected value of the equation 3 and thus find the gain solutions for the NONE, SIMPLE and FULL corrections. As an additional step, we check the shape of the distribution of 8; in case it is not Gaussian, no truncation is made to the distribution, and the expected value of the equation 3 is calculated with arithmetic mean.

3.3 No linearity Correction

To see the effect of linearity correction on the shape of the PTC and its parameters, we used a Spline linearizer with 12 nodes for detectors 32 (ITL) and 139 (E2V). This linearizer was generated by Jeronimo⁵ and in his analysis found that a Spline with 12 equally spaced nodes greatly corrects the effect of the nonlinearity and decreases the dispersion in the residuals. All configurations were the same, except, of course, the linearity correction (see table 1).

Table 1: Configuration used to generate the PTCs. The linearity correction is performed in this case, “doLinearize: true”.

Configuración			
doWrite: true	doLinearize: true	doFlat: false	doInterpolate: false
doOverscan: true	doCrosstalk: false	doFringe: false	doSaturation: false
doAssembleCcd: true	doBrighterFatter: false	doApplyGains: false	doSaturationInterpolation: false
doBias: true	doDark: true	doDefect: true	growSaturationFootprintSize: 0
doVariance: true	doStrayLight: false	doNaNMasking: true	ptcFitType: EXPAPPROXIMATION

Subsequently, plots of $\frac{Variance}{Mean}$ vs $Mean$ are constructed, so that the variance is normalized. Thus, it is analyzed whether the bump between 50000 and 60000 ADU is corrected. In addition, a relative percentage

⁵Jerónimo was my partner during this internship, who worked on the sister project Study of the Linearity of the CCDs of the Vera C. Rubin Observatory

error between the parameters obtained from the PTC fit with and without correction for linearity is calculated to quantify the effect on these. Finally, we checked whether the parameters and/or the shape of the PTC changed concerning its version without correction for nonlinearity.

3.4 Crosstalk Correction

The full focal plane readout of the LSSTCam can reach a readout time of 2s, so the combination of high speed, high resistivity silicon components, and close spacing between each channel makes the LSSTCam more susceptible than any other mosaic camera to electronic crosstalk (O'Connor, 2015).

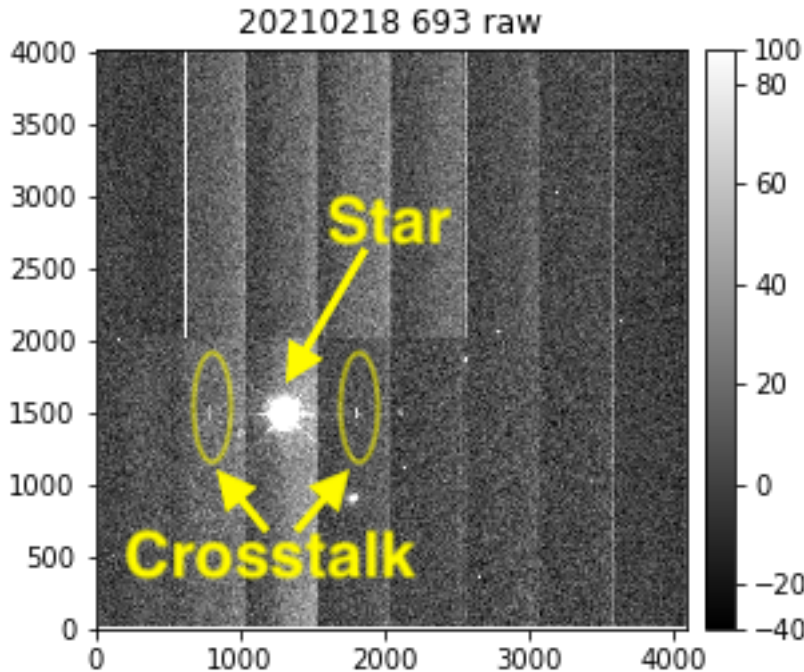


Figure 9: Image of a bright star taken with the 1.2m auxiliary telescope at the Vera Rubin Observatory. Segments adjacent to the bright start image show crosstalk.

Electronic crosstalk occurs in CCDs that contain several channels that are read simultaneously and coupled so that a channel that detects a bright source will cause a ghost image to be generated in adjacent segments due to this coupling (Snyder et al., 2020). This effect is presented in figure 9, where “ghost” signals are observed in the lateral segments of the detector. Figure 10 shows a heat map on the left for ITL detector 32 and on the right for ITL detector 139, where the highest crosstalk coefficients are in blue colors, and it is observed that the crosstalk pattern is different per vendor. These same coefficients are entered into a configuration file in the LSST software to re-generate the PTC with this correction.

Finally, as in the section 3.3, we checked whether the parameters and/or the shape of the PTC changed concerning its version without correction for crosstalk.

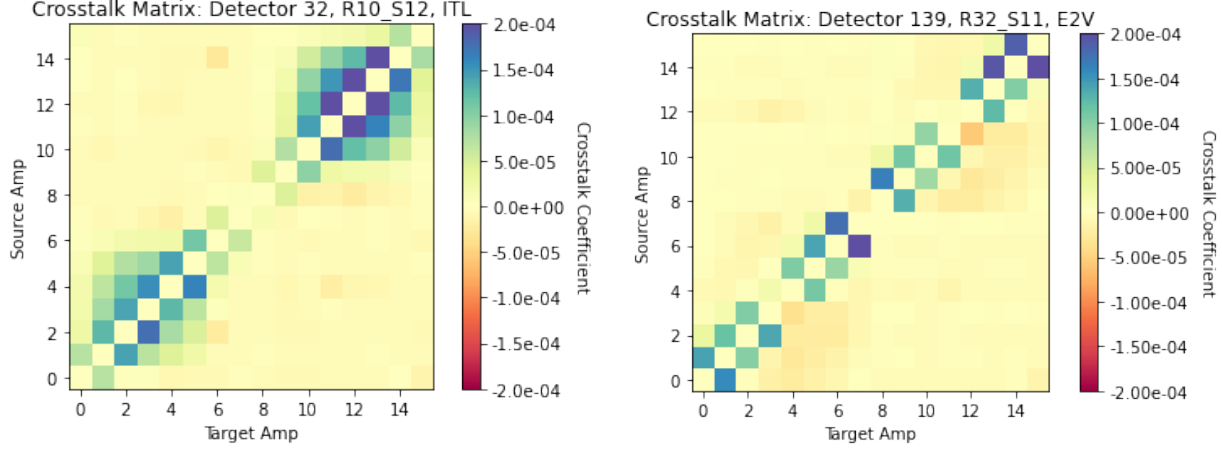


Figure 10: Crosstalk matrix on the left for detector 32 (ITL) and on the right for 139 (E2V).

4 Results

4.1 PTC

As part of this project, an initial and fundamental task was to use the PTC to determine the essential parameters of each CCD segment across the focal plane, using the *DM stack*. This has already been done by SLAC National Acceleration Laboratory⁶ (hereafter SLAC) for this very run (SLAC heat maps BOT 13144) and here we seek to reproduce their results.

Initially, we generated the PTCs by CCD for the entire focal plane, as shown in Figure 11, to detect PTCs with abnormal behavior and low PTC-turnoff (below 40000 ADU). Detectors found with low PTC-turnoff and/or misclassified are recorded in the table 2. In addition, a visual inspection showed that about 60 % of the detectors have at least one segment showing *Downing dip*.

Subsequently, we generate heat maps for the entire focal plane similar to those performed by SLAC, shown in the panels of Figure 12, for the parameters estimated by the fit to the PTC: gain and read noise in the upper left and right panel, respectively; a_{00} and turnoff in the lower left and right panel, respectively. A bimodality is found in the gain and a_{00} value (which accounts for the B-F effect); the more reddish values dominate in the E2V sensors, while the more yellow values dominate in ITL; this means that the E2V vendor's detectors have in general a lower gain, but a more negative B-F effect coefficient concerning ITL. Whereas, for readout noise and turnoff, no relevant effect is exhibited due to the vendor.

El comportamiento descrito anteriormente por los mapas de calor son reforzados por los histogramas de la figura 13, los cuales revelan la clara bimodalidad para la ganancia y a_{00} y un comportamiento más generalizado para el ruido de lectura y el turnoff. La ganancia tiene un valor promedio para los sensores de E2V de 1.49 ± 0.05 y de 1.69 ± 0.05 e^-/ADU para ITL. El coeficiente del B-F effect tiene un valor medio de $(-3.0 \pm 0.1) \times 10^{-6}$ y $(-1.7 \pm 0.2) \times 10^{-6}$ para E2V e ITL, respectivamente.

⁶El código utilizado por SLAC está disponible en SLAC code

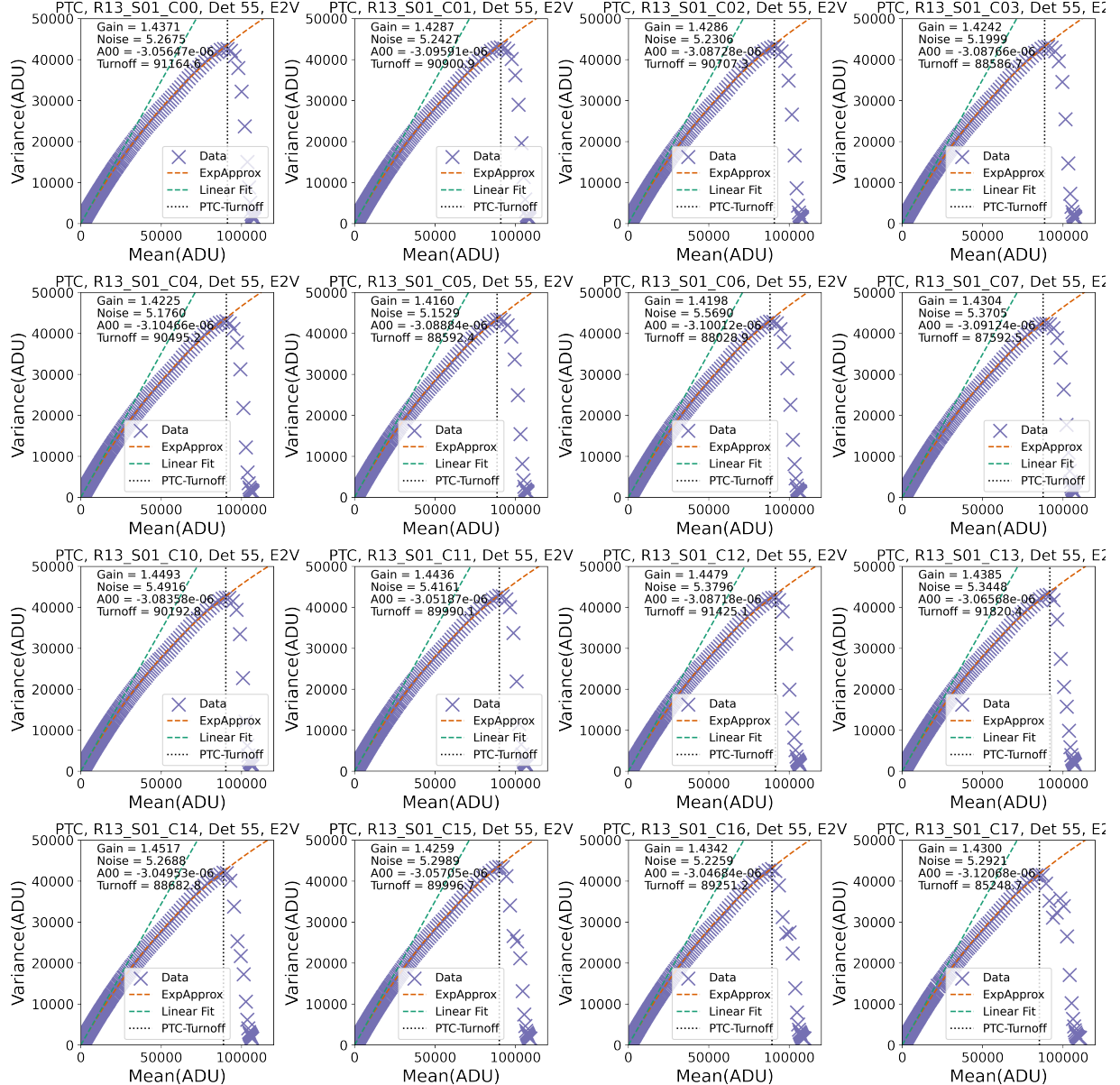


Figure 11: PTC for all segments of sensor 55 (E2V). Xs represent the data, the red line is the fit to the PTC by exponential approximation (eq. 1), and the green line is a linear fit. The parameters obtained from the fit to the PTC are the gain, the a_{00} parameter, the PTC turnoff (Max ADU), and the read noise.

The histograms support the behavior described above by the heat maps in Figure 13, which reveal clear bimodality for gain and a_{00} and more generalized behavior for read noise and turnoff. The gain has an

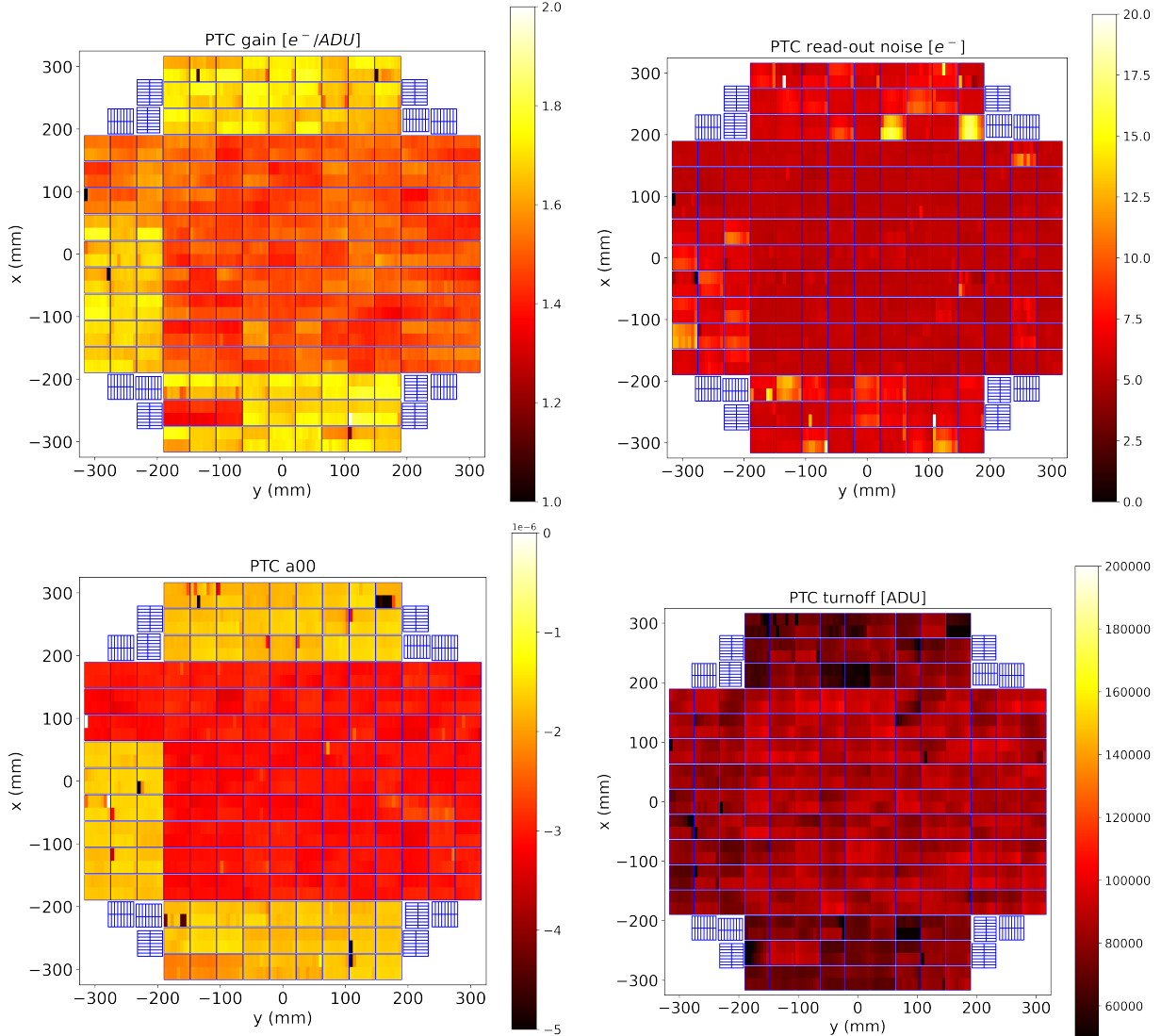


Figure 12: Heatmaps for the entire focal plane of the parameters obtained by the fit to the PTC in each segment that makes up the sensors. The upper panel shows the gain values on the left and the read noise on the right. The lower panel shows on the left the values of a_{00} , which are of the order of -1×10^{-6} , and on the right, the turnoff. These maps are a reproduction of those already constructed by SLAC for this same run 13144 (SLAC heat maps).

average value for the E2V sensors of 1.49 ± 0.05 and $1.69 \pm 0.05 e^- / ADU$ for ITL. The BF effect coefficient has an average value of $(-3.0 \pm 0.1) \times 10^{-6}$ and $(-1.7 \pm 0.2) \times 10^{-6}$ for E2V and ITL, respectively.

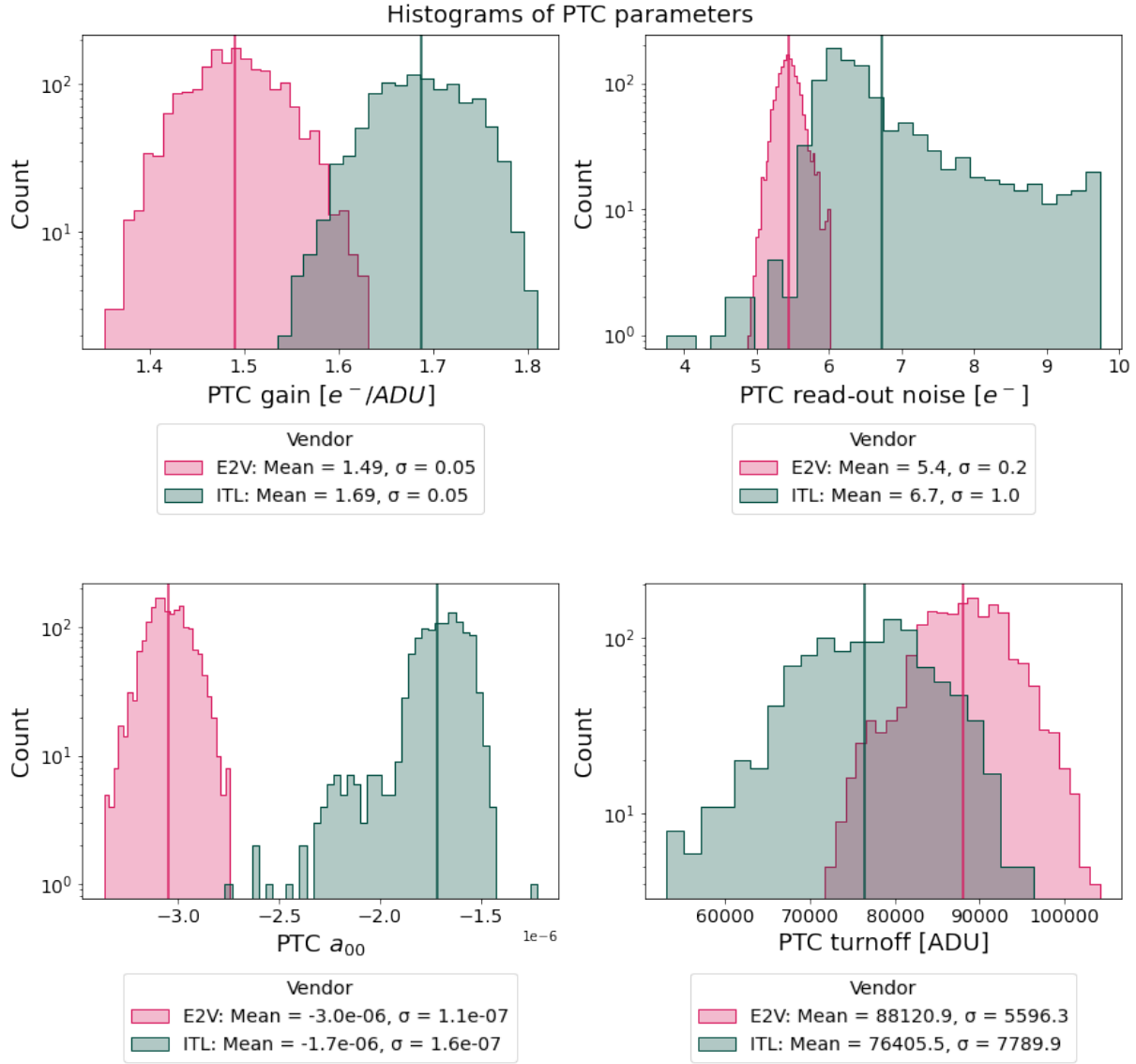


Figure 13: Histograms for the parameters obtained from the fit to the PTC: gain (top left), read noise (top right), a_{00} (bottom left), and turnoff (bottom right), each of the distributions are shown by vendor, in magenta for E2V and blue for ITL. The vertical lines represent the mean of each distribution.

Although, in general, the results between this work and SLAC are congruent, we find differences in some segments for gain, especially in segments C04 and C14 of detector 0 (R01_S00), C00 of detector 22

(R03_S11) and C02 of detector 169 (R41_S21). In table 2 we report in red the segments where we found the most notorious difference between our and the SLAC results for the four parameters (gain, BF coefficient, read noise, and turnoff). For the segments mentioned above, the table shows that detector 22 is possibly dead; in contrast, for the segment of detector 169, there is a misclassification by the PTC-turnoff location algorithm. For these particular segments, the before mentioned can be the reason for the difference between SLAC and us. However, to determine which is causing the differences precisely, it is necessary to conduct a detailed analysis of the respective codes used and their versions. Differences between the algorithms may lead to these differences because we used the same run (13144). It can be differences in the pixels used for the calculation due to the masks used, differences in the reduction of the images (Instrument Signature Removal or ISR), or different rejection of outliers, among others.

```

206      # Cannot assume that the mean values are sorted
207      ptc_turnoff = max(mean[index])

(a) Eotest code

839      # Discard points when the variance starts to decrease after two
840      # consecutive signal levels
841      goodPoints = self._getInitialGoodPoints(meanVecOriginal, varVecOriginal,
842                                         self.config.minVarPivotSearch,
843                                         self.config.consecutivePointsVarDecreases)
844

857      # Save the point where the variance starts decreasing as the
858      # PTC turnoff point
859      ptcTurnoff = meanVecOriginal[goodPoints][-1]
860      dataset.ptcTurnoff[ampName] = ptcTurnoff

(b) DM stack code

```

Figure 14: Codes used to calculate the PTC-turnoff in eotest (a), used by SLAC, and DM stack (b), official code for LSST data.

For the turn-off, we generally observed similar behavior for the sensors between this work and SLAC. However, the way of determination used different methods, as shown in figure 14. On the one hand, *eotest* defines the PTC-turnoff as the point where the variance is maximum, where the maximum value is determined among the data whose residuals are below 5σ . In contrast, *DM stack* defines this as the point where the variance starts to decrease monotonically by at least two points (the number of points to decrease can be modified in the function `_getInitialGoodPoints`). By SLAC, the FWC found was ~ 90000 e⁻ **referencia?**. In contrast, in this work, we found an average value of turnoff with a value of 83240 ADU, whose equivalence in electrons would be an approximate value of the FWC of 130000 ± 10000 e⁻.

Table 2: Detectors containing segments with low PTC-turnoff (below 40000 ADU), PTC-turnoff misclassified by the algorithm, bad segments, or differences observed concerning the results obtained by SLAC (parameters in red). Presented for each segment is the detector ID (col1), detector number (col2), vendor (col3), affected segment (col4), PTC parameters (gain, B-F effect, and turnoff coefficient; cols 5, 6, 7, and 8, respectively), detected problem (col9).

Detector ID	Det Num	Vendor	Amp	Gain [e^-/ADU]	Read Noise [e^-]	A_{00}	Turnoff [ADU]	Issue
R01_S00	0	ITL	C04	1.5833	6.2061	-2.0160 $\times 10^{-6}$	73461.2	SLAC diff
R01_S00	0	ITL	C14	1.7514	6.4150	-2.1907 $\times 10^{-6}$	68032.3	SLAC diff
R01_S20	6	ITL	C00	1.5354	11.1174	-4.1734 $\times 10^{-6}$	65371.7	SLAC diff
R01_S20	6	ITL	C05	1.4837	15.5104	-4.5175 $\times 10^{-6}$	76106.5	SLAC diff
R01_S20	6	ITL	C06	1.5104	13.5644	-4.3955 $\times 10^{-6}$	72293.9	SLAC diff
R02_S20	15	ITL	C17	1.67191	5.81973	-2.20396 $\times 10^{-6}$	30567.4	low PTC-turnoff
R03_S11	22	ITL	C00	15.2117	44.0087	-0.708105	223.072	SLAC diff - dead?
R10_S11	31	ITL	C10	1.63413	4.13177	-3.65785 $\times 10^{-6}$	32842.4	low PTC-turnoff
R20_S00	72	ITL	C17	0	0	nan	0	SLAC diff and dead
R20_S01	73	ITL	C00	1.6083	6.45279	-3.12539 $\times 10^{-6}$	35507.4	low PTC-turnoff
R20_S12	77	ITL	C00	1.59232	4.70427	-8.02249 $\times 10^{-6}$	26827.1	low PTC-turnoff
R30_S00	117	E'2V	C10	0	0	nan	0	SLAC diff and dead
R41_S20	168	ITL	C16	1.61074	6.07818	-1.98753 $\times 10^{-6}$	37863.2	low PTC-turnoff
R41_S20	168	ITL	C17	1.59228	9.57256	-2.54637 $\times 10^{-6}$	26120	low PTC-turnoff
R41_S21	169	ITL	C02	1.08095	62.8775	-4.52943 $\times 10^{-6}$	16237.9	SLAC diff and PTC-turnoff mismatch
R41_S21	169	ITL	C11	1.61255	5.23312	-2.61051 $\times 10^{-6}$	32467.3	PTC-turnoff mismatch
R41_S21	169	ITL	C15	1.59804	5.21757	-2.31531 $\times 10^{-6}$	39151.3	PTC-turnoff mismatch
R41_S22	170	ITL	C10	1.60171	4.76741	-3.2105 $\times 10^{-6}$	32369.9	low PTC-turnoff
R42_S00	171	ITL	C17	1.6516	6.4254	-3.09362 $\times 10^{-6}$	30253.3	low PTC-turnoff
R43_S10	183	ITL	C17	1.59721	8.53352	-2.46596 $\times 10^{-6}$	30195.2	low PTC-turnoff
R43_S22	188	ITL	C00	1.6348	5.28826	-4.64678 $\times 10^{-6}$	21477.5	SLAC diff
R43_S22	188	ITL	C01	1.6348	5.28826	-4.64678 $\times 10^{-6}$	21477.5	low PTC-turnoff
R43_S22	188	ITL	C02	1.55382	6.94625	-7.40255 $\times 10^{-6}$	30764.3	low PTC-turnoff
R43_S22	188	ITL	C03	1.56826	7.24918	-4.92713 $\times 10^{-6}$	38222.4	low PTC-turnoff
R43_S22	188	ITL	C04	1.58147	3.76291	-4.88158 $\times 10^{-6}$	38143.6	low PTC-turnoff

4.2 Gain from flat pairs

Initially, we used the PTC to obtain the gain. However, this method requires more time to be generated since it is a fit over an extensive range in flow. Therefore, we have an alternative approach, which we will call *gain by pairs of flats*, less time-consuming. The left panel of the figure 15 shows for detector 55 the gain values in a range of flux between 0 to ~ 120000 ADU, which includes values that have exceeded the saturation level given by the vertical lines marking the PTC-turnoff for each segment. On the right panel, the gain values are only a little further away from the saturation level, and we can see a bump around 60000 ADU due to the nonlinearity, which will be discussed in section 4.3. It is worth mentioning that we only use data below the PTC-turnoff for the analysis of the gain per pair of flats.

In this section, we describe the differences we found between the gain by PTC and pairs of flats, a possible way to decrease them, and finally, what to expect from this second method concerning the first one.

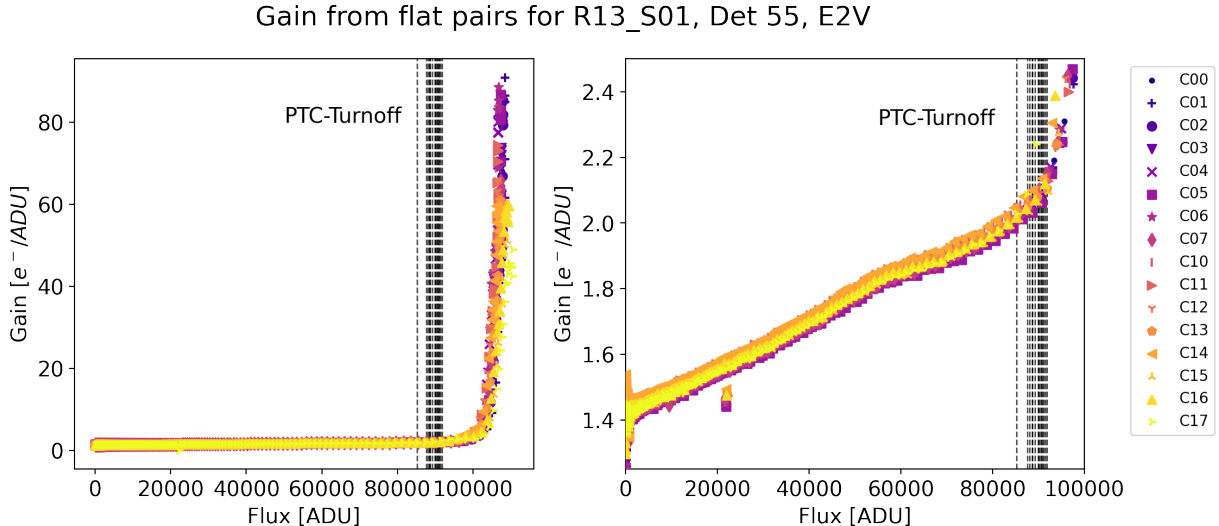


Figure 15: Gain values obtained by flat pairs for fluxes up to approximately 120000 ADU for detector 55 (R13_S01). In both panels, the dashed vertical lines represent the PTC turnoff value for each of the 16 detector segments, and the colored figures represent the gain and flux values for each segment. The right panel shows only the region up to the PTC-turnoff of the left panel.

As we mentioned in the methodology (sec. 3), we used two code versions (`w_2022_27` and `w_2022_32`), where the main difference and our interests is the one shown in figure 16. This figure shows how the two code versions handled the statistics to compute gain by pairs of flats. The `w_2022_27` version used the red code with the assumption of a Gaussian distribution, so it truncates the distribution to reject outliers. Whereas the `w_2022_32` version used the green code rejecting the before assumption. The last one is our recommendation due to the analysis results described in this section. In short: the distribution of the operation between two flats images leading to calculating the gain does not have a Gaussian distribution, so performing a truncation in the distribution alters the expected value for the gain.

```

@@ -758,7 +758,7 @@ def getGainFromFlatPair(self, im1Area, im2Area, imStatsCtrl, mu1, mu2,
758   758
759   759     ratioIm /= sumIm
760   760
761 -   const = afwMath.makeStatistics(ratioIm, afwMath.MEANCLIP, imStatsCtrl).getValue()
761 +   const = afwMath.makeStatistics(ratioIm, afwMath.MEAN, imStatsCtrl).getValue()
762   762     gain = 1. / const
763   763
764 -   if correctionType == 'SIMPLE':
764 +   if correctionType == 'SIMPLE':

```

Figure 16: Difference between the initial(w_2022_27, in red) and current (w_2022_32, in green) codes for calculating the gain from a pair of flat fields.

The version *w2022* gave us the result shown in figure 6, a relative percentage error between the gain per PTC and flat pair at a flux of 5000 ADU above 5 %, the same result for an E2V detector (upper panel) and an ITL detector (lower panel). This high percentage at this flux was not expected, so we performed simulations with the methodology described in section 3.2.1 to investigate what was generating this value.

4.2.1 Simulation

From the previous result, a relative error between the gains of 5 % at 5000 ADU, we had some hypotheses: first, the masks in the flat images could be affecting in some way, e.g., if the masks of each image are very different and the code uses these to make calculations, it could generate a high relative error; second, an overestimation in the read noise; and third, if it is not the masks, so what in the statistics is causing this error.

We found from simulations of a flat image of a CCD segment and using the mask of an actual segment: the use of one mask for the two flats, the union of both masks, or different masks for each do not account for the error of 5 % at 5000 ADU, as shown in the top panel of Figure 17. We notice in this case that the higher the read noise, when using a NONE type correction, the more significant the discrepancies between the expected and calculated gain ($2 e^-/\text{ADU}$). However, the subsequent corrections (SIMPLE and FULL), which account for the read noise, accurately calculate the expected gain value. Nonetheless, the bottom panel of this figure, which includes, besides the masks, the control statistics, gives an account in all cases of a relative percentage error between the gain per PTC and flats pairs above 5 %. In the next section (4.2.2) we check this with the real data.

4.2.2 Real data

Because of the results obtained from the simulation, we checked whether the results held with the actual data, and indeed they did. We performed this check on detector 55 (R13_S01) for all its segments, as shown in figures 18 and 19, where the black crosses represent the gain value obtained from the PTC. The first figure again reveals that the masks and no control statistics do not account for a relative error more significant than 5 % for any segment of the detector; indeed, the maximum value achieved is 2.25 % at an average flux of 5450 ADU. In the before result, we used the same mask for calculations: the union of the individual masks. The second figure, which uses the masks and incorporates the control statistics, shows that the handling of the statistics is producing high discrepancies between the gain by PTC and pairs of

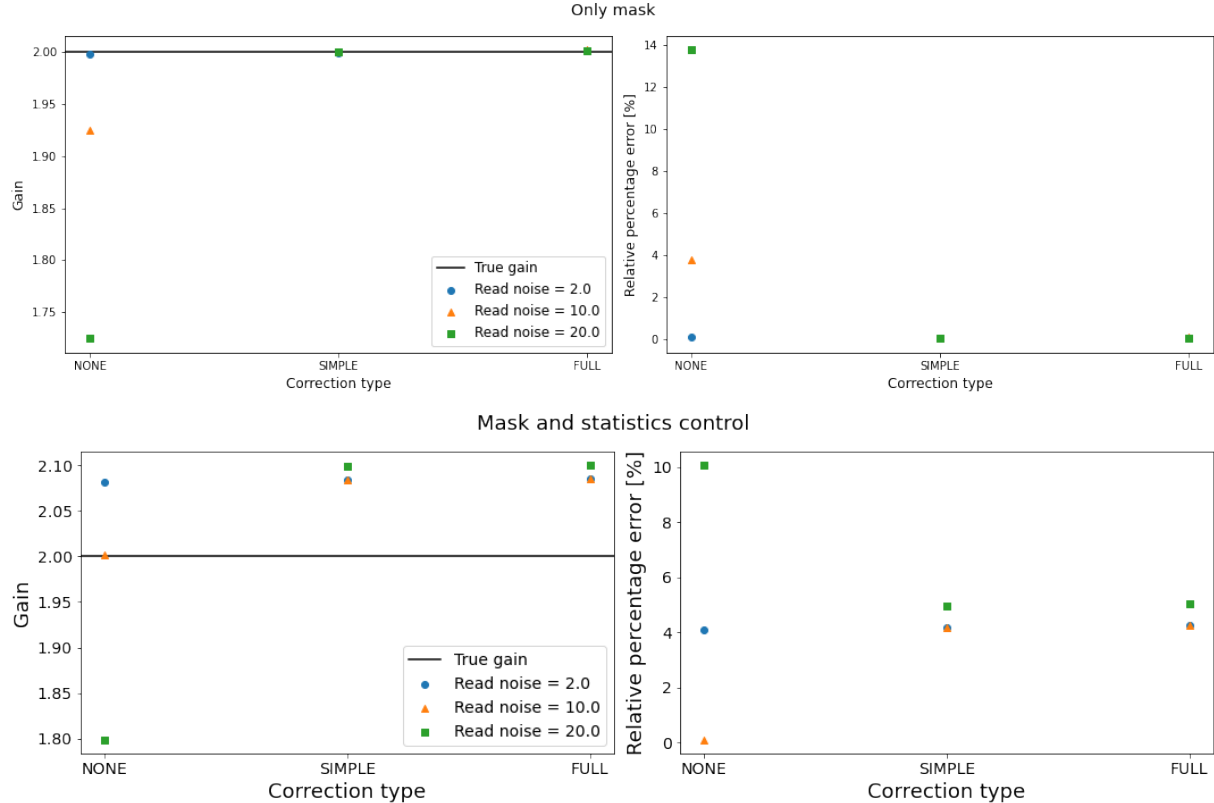


Figure 17: Simulation results to obtain the gain per pair of flats in the upper panel using only masks and in the lower panel adding control statistics. The average flux value of these simulated flats is 5000. The left panels show the gain value for three different models, and on the right, the relative percent error concerning the expected gain value, $2 e^-/\text{ADU}$. In the left panels, the horizontal black line represents the predicted gain value, and the figures represent the different values considered for the read noise: the blue circle of $2 e^-$, the orange triangle of $10 e^-$, and the green square of $20e^-$. Considering these read noises, we calculated the gain for three models: NONE, SIMPLE and FULL.

flats, reaching differences of up to 9 % in one of the segments at a flow rate of 5450 ADU.

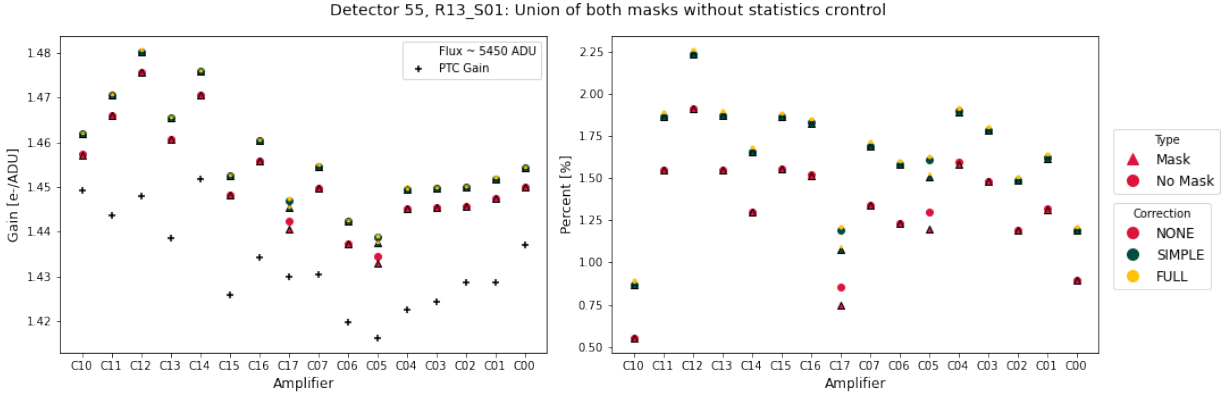


Figure 18: Gain value on the left panel and the relative percentage error on the right panel for the 16 segments (amplifiers) of detector 55 (R13_S01). In the left panel, the black crosses represent the value of the gain per PTC. For both panels, the figures represent whether the calculation of the gain from flat pairs used mask (triangles) or not (circles) and the colors are associated with the model used to determine the gain: NONE (red), SIMPLE (green) and FULL (yellow). The mask for calculation was the union of the masks of both flat images per segment, and we did not use control statistics.

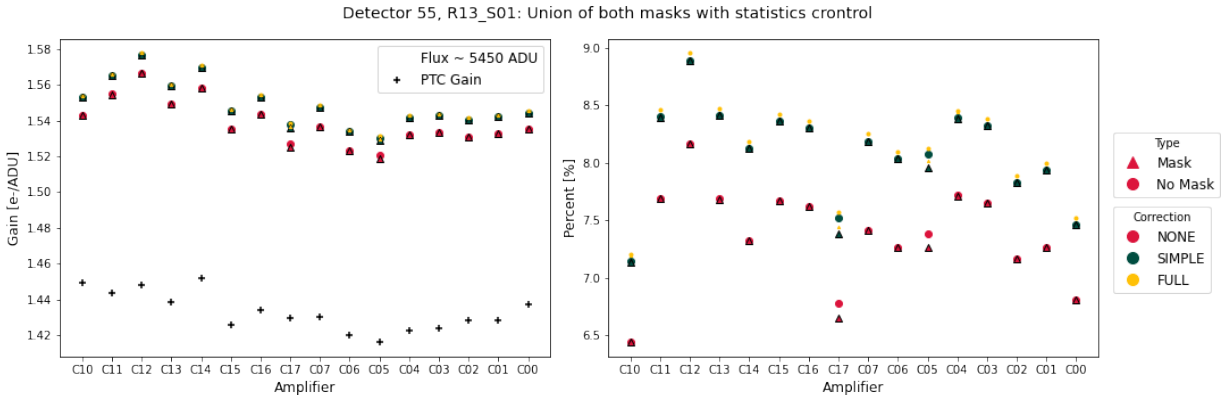


Figure 19: See description of the figure 18. This figure used control statistics.

Subsequently, we performed plots of the distributions for the operation between the flats images given by the equation 8, which is the argument of the Lupton equation (eq. 3) and is directly related to the gain. The results we obtained are shown in figure 20 for each detector segment and reveal that the shape of this distribution is far from Gaussian. So truncating this distribution produces a change in the mean value, which no longer coincides with the mean of the original distribution, thus giving a different gain value than expected.

Finally, we again constructed the relative percentage error figures for the gain without truncating the distribution, as shown by the green code in figure 16. We obtained the result in figure 21, which reveals in

its embedded image that for a flow of 5000 ADU, the difference between the two gains is now below 5 %, as indicated by the simulations. With this result, we estimate a general relationship for the gain taking into account the distributions for the linear fit parameters, as shown in figure 22, which was performed between 5000 and 10000 ADU. In this figure, we can see on the top left the distribution of the slopes by the vendor, which reveals a clear bimodality, with the E2V detectors having a slightly higher slope concerning ITL, with a mean of (0.00046 ± 0.00004) and (0.00027 ± 0.00004) %/ADU, respectively. In the bottom panel of this figure, we have the intercept with the y-axis (i.e., with the percentage error axis between the gains), and it shows that there is an overall mean across the detectors, with no appreciable distinction by vendor, with a value of (-0.5 ± 0.5) %. Thus, by vendor, the relative percentage error between the 5000 and 1000 ADU is given by

- E2V: $Error_{2Gain} = (0.00046 \pm 0.00004)F - (0.5 \pm 0.5)$, where the error interval is $(1.8 \pm 0.7, 4.1 \pm 0.9)$ %.
- ITL: $Error_{2Gain} = (0.00027 \pm 0.00004)F - (0.5 \pm 0.5)$, where the error interval is $(0.85 \pm 0.7, 2.2 \pm 0.9)$ %.

4.3 Crosstalk and non linearity correction

A part of the final analyses we performed during this internship consisted of quantifying and deciding whether the crosstalk effect and the nonlinearity impact the shape of the PTC and/or the fundamental parameters: gain, read noise, B-F effect, and turnoff coefficient.

As described in section 3.4, we had access to the crosstalk matrices for detector 32 (ITL) and 139 (E2V), which are shown in Figure 10. We obtained from applying the methodology of that section that the differences between PTC with and without crosstalk correction are shallow, as shown in Figure 23 and Figure 24. They illustrated that considering the region below saturation, the difference between the variances is consistently below 0.1 ADU. In contrast, the most significant variance in the parameters is $\sim 0.1\%$ in read noise and BF effect coefficient and $\sim 0.07\%$ in gain and turnoff. The most significant differences were found in the ITL detector segments. According to the above, we conclude that the crosstalk does not have a considerable effect. So, correcting this effect is unnecessary since the difference in the parameters is small and does not alter the shape of the PTC.

Finally, the 12-node cubic spline linearizer was applied to verify its impact on the PTC shape. The result of correcting only for crosstalk (orange dots), only for nonlinearity (blue diamonds), corrected for both effects (gray triangles), and the uncorrected data (magenta squares) is presented in Figure 25. We see that the uncorrected data show a bump around 60000 ADU, while the crosstalk-corrected data are always located at the same position as the uncorrected data (thus also showing the bump), the data corrected for nonlinearity flatten it. Accordingly, making both corrections to the data has no more significant effect than fixing for nonlinearity alone. Again we find that the crosstalk is not a necessary correction since it does not affect either the shape or the parameters of the PTC.

5 Conclusions

We present in this report a list of the sensors that present differences in the parameters with those obtained by SLAC, a PTC with low turnoff, and an inadequate classification of the same so that they can be reviewed

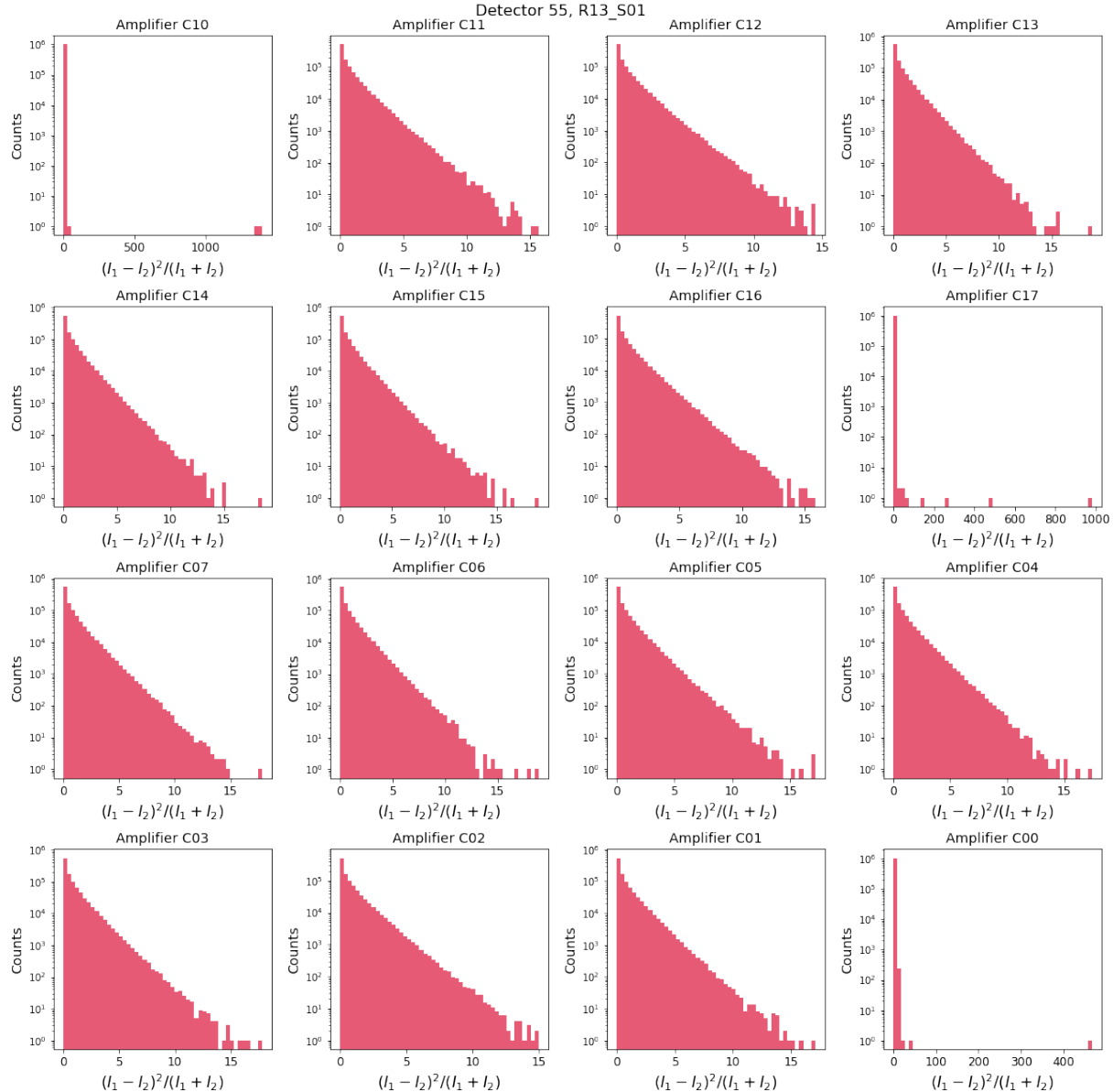


Figure 20: Histogram of the distribution for $\frac{(I_1 - I_2)^2}{I_1 + I_2}$ for each segment of detector 55 (R13_S01).

later. We use the default value to determine the turnoff via *DM stack*: decrease by at least 2 points to indicate shutdown.

We find in the PTC study that there is a bimodality per vendor for gain and a_{00} and a more generalized

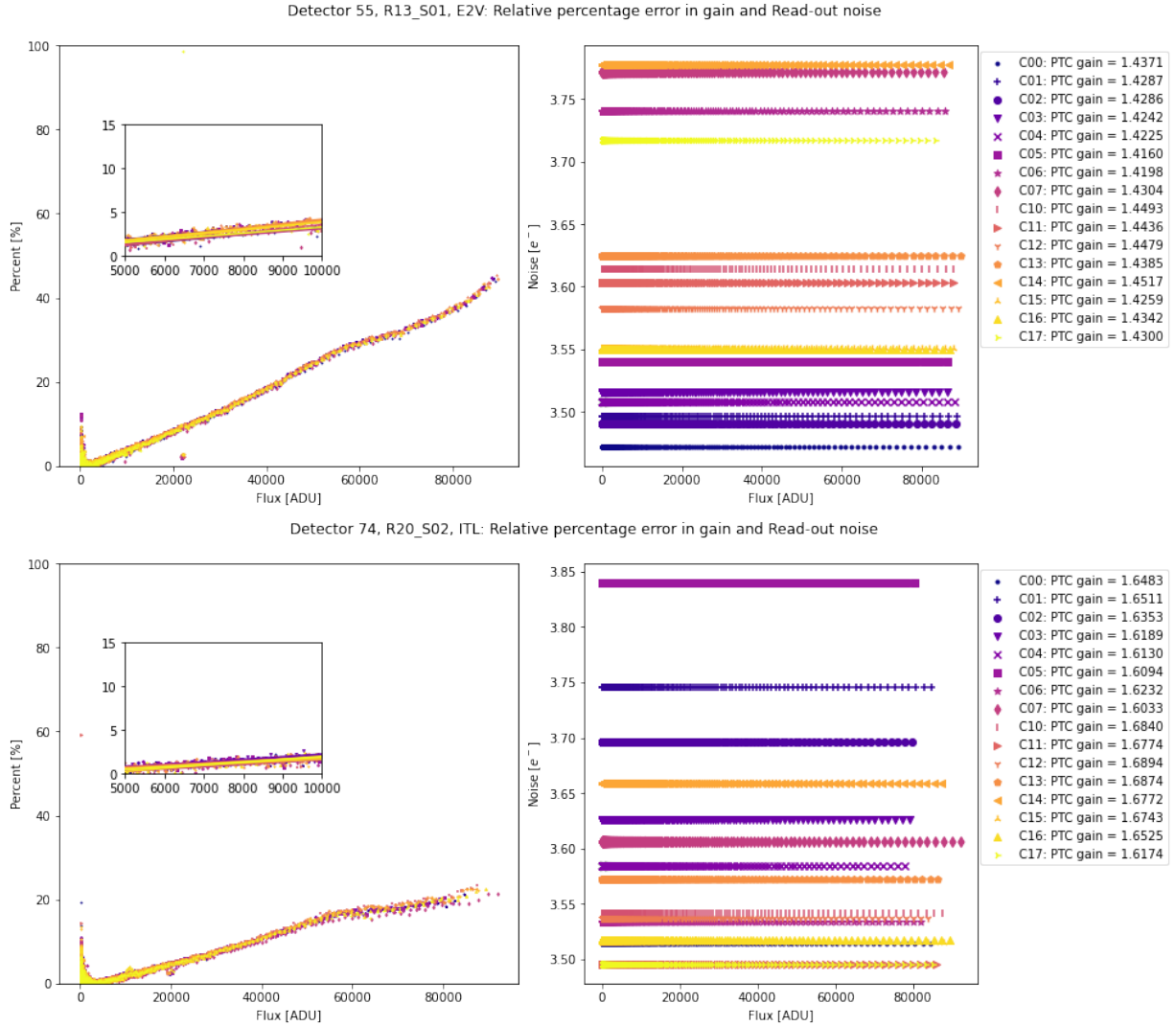


Figure 21: Refer to the description of the figure 6. This plot uses the updated code (version w_2022_32) that does not use clipped mean.

behavior for read noise and turnoff. The average value we found for the gain in the E2V sensors of 1.49 ± 0.05 and 1.69 ± 0.05 e^-/ADU for ITL. The coefficient of the BF effect has an average value of $(-3.0 \pm 0.1) \times 10^{-6}$ and $(-1.7 \pm 0.2) \times 10^{-6}$ for E2V and ITL, respectively. In addition, ITL detectors present a higher read noise dispersion compared to E2V (6.7 ± 1.0 e^- and 5.4 ± 0.2 e^- , respectively). The results obtained in this work are generally congruent with those obtained by SLAC. However, the main difference was observed in the Full Well Capacity value: in this work, we found a value of 130000 ± 10000 e^- , while SLAC a value of

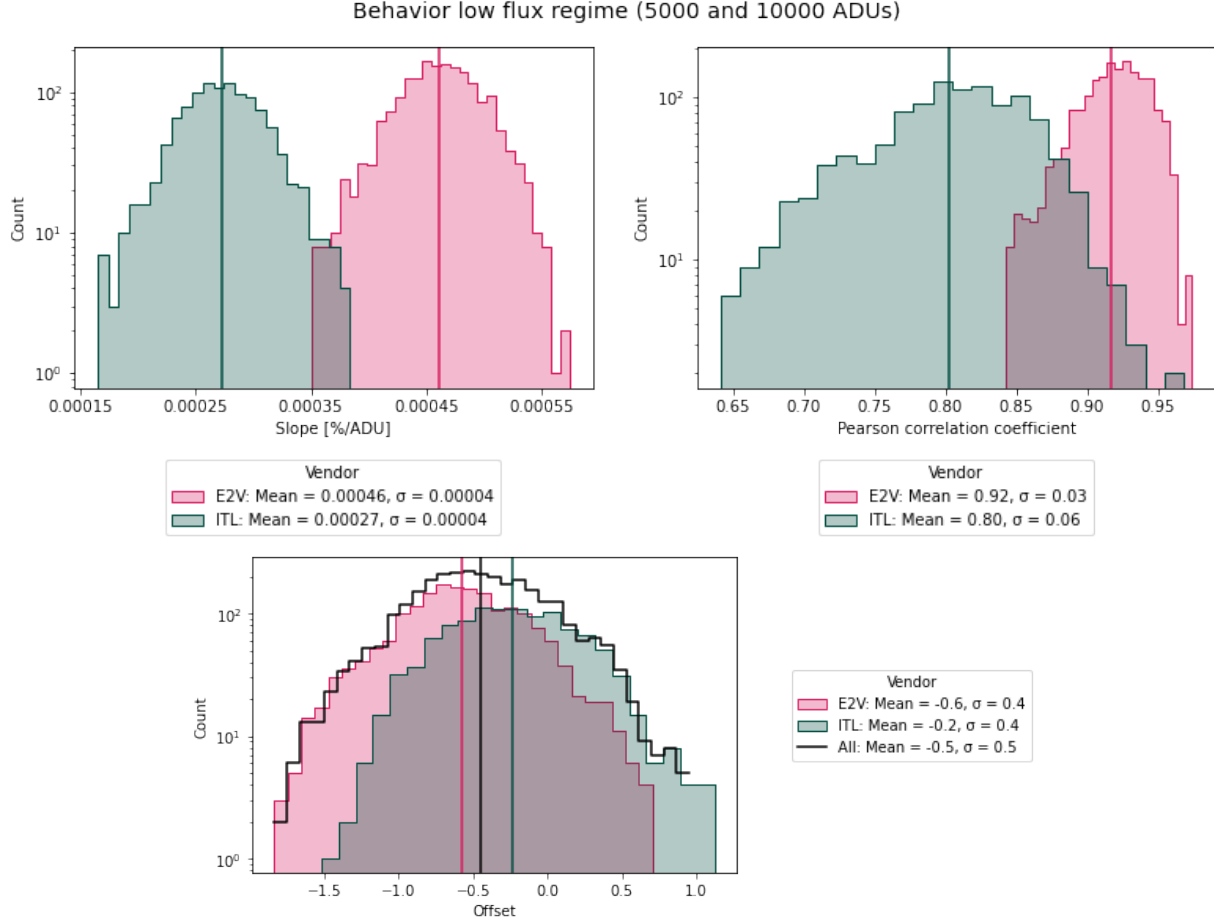


Figure 22: Histograms for the slope (top left), Pearson’s correlation coefficient (top right), and the y-axis intercept (bottom panel) corresponding to the linear fit performed in the flow region between 5000 and 10000 ADU for the gain. Its construction used the updated code (version w_2022_32), and the colors represent the vendor, E2V in red and ITL in blue. The vertical lines represent the mean for each case.

90000 e⁻, which is a product of the different ways of calculating the turnoff between *eotest* and *DM stack*.

The analysis between the gain obtained from a pair of flats and the gain obtained from the PTC initially yielded a relative percentage error for low fluxes (5K and 10K ADU) higher than 5%. This result led to a thorough investigation of its origin, finding that the distribution following the Lupton equation for flat images is not of Gaussian type, so the truncation of the distribution to calculate the statistics generating a shift of the mean value, and consequently, larger values of gain concerning the PTC gain. Therefore, this calculation was performed without truncation and obtained percentage differences between these two gains of $(1.8 \pm 0.7, 4.1 \pm 0.9)$ for E2V and $(0.85 \pm 0.7, 2.2 \pm 0.9)$ for ITL, where these intervals correspond

to a flow region between 5000 and 10000 ADU. Consequently, the respective report was made and finally implemented in the main code.

Finally, the linearity correction fixes the observed bump around 50K-60K ADU. Whereas performing a correction for crosstalk does not affect the shape of the PTC, nor does it significantly modify the parameters. Therefore, we recommend correcting for linearity only.

6 Acknowledgments

First, I want to thank the entire RECA internship program team, who saw the need for this program and made the possible growth in research Colombia's students, providing a great learning experience, both computational and observational. To LSSST Corporation, which financed the realization of this project. To my advisers, Drs. Andrés M. Plazas & Craig Lage, who were the guide throughout this learning process, were willing to answer any questions and shared a little about their lives, making a closer relationship despite the virtuality. Finally, thanks to my colleague Jerónimo Calderón for the discussions, and feedback throughout the project.

References

- Astier, P., Antilogus, P., Juramy, C., Le Breton, R., Le Guillou, L., & Sepulveda, E. (2019). The shape of the photon transfer curve of ccd sensors. *Astronomy & Astrophysics*, 629, A36.
- Astropy Collaboration, Price-Whelan, A. M., Sipőcz, B., Günther, H., Lim, P., Crawford, S., ... others (2018). The astropy project: building an open-science project and status of the v2. 0 core package. *The Astronomical Journal*, 156(3), 123.
- Burkardt, J. (2014). The truncated normal distribution. *Department of Scientific Computing Website, Florida State University*, 1, 35.
- Coulton, W. R., Armstrong, R., Smith, K. M., Lupton, R. H., & Spergel, D. N. (2018). Exploring the brighter-fatter effect with the hyper suprime-cam. *The Astronomical Journal*, 155(6), 258.
- Downing, M., Baade, D., Sinclair, P., Deiries, S., & Christen, F. (2006). Ccd riddle: a) signal vs time: linear; b) signal vs variance: non-linear. In *High energy, optical, and infrared detectors for astronomy ii* (Vol. 6276, pp. 76–86).
- Harris, C. R., Millman, K. J., Van Der Walt, S. J., Gommers, R., Virtanen, P., Cournapeau, D., ... others (2020). Array programming with numpy. *Nature*, 585(7825), 357–362.
- Ivezić, Ž., Kahn, S. M., Tyson, J. A., Abel, B., Acosta, E., Allsman, R., ... others (2019). LSST: from science drivers to reference design and anticipated data products. *The Astrophysical Journal*, 873(2), 111.
- Koren, M. (2020). *An influential female astronomer is getting her due.* Retrieved from <https://www.lsst.org/sites/default/files/sites/default/files/docs/Vera%20Rubin%20Well-Deserved%20Space%20Observatory%20-%20The%20Atlantic.pdf>
- Lage, C., Bradshaw, A., & Tyson, J. A. (2017). Measurements and simulations of the brighter-fatter effect in ccd sensors. *Journal of Instrumentation*, 12(03), C03091.
- LSST Science Collaboration, Abell, P. A., Allison, J., Anderson, S. F., Andrew, J. R., Angel, J. R. P., ... et al. (2009, December). LSST Science Book, Version 2.0. *ArXiv e-prints*.
- Lupton, R. H. (2014). Consequences of thick ccds on image processing. *Journal of Instrumentation*, 9(04), C04023.

- Newbry, S., Lange, T., Roodman, A., Reil, K., Bond, T., Rasmussen, A., ... Lee, V. (2018). Lsst camera bench for optical testing: design, assembly, and preliminary testing. In *Ground-based and airborne instrumentation for astronomy vii* (Vol. 10702, pp. 1553–1571).
- NSF. (2020). Nsf-supported observatory renamed for astronomer vera c. rubin. *National Science Foundation*. Retrieved from <https://beta.nsf.gov/news/nsf-supported-observatory-renamed-astronomer-vera>
- O'Connor, P. (2015). Crosstalk in multi-output ccds for lsst. *Journal of Instrumentation*, 10(05), C05010.
- Rubin, V. C. (2011). An interesting voyage. *Annual Review of Astronomy and Astrophysics*, 49, 1–28.
- Snyder, A., Barrau, A., Bradshaw, A., Bowdish, B., Chiang, J., Combet, C., ... others (2020). Laboratory measurements of instrumental signatures of the lsst camera focal plane. In *X-ray, optical, and infrared detectors for astronomy ix* (Vol. 11454, pp. 649–669).
- Walter, C. (2015). The brighter-fatter and other sensor effects in ccd simulations for precision astronomy. *Journal of Instrumentation*, 10(05), C05015.

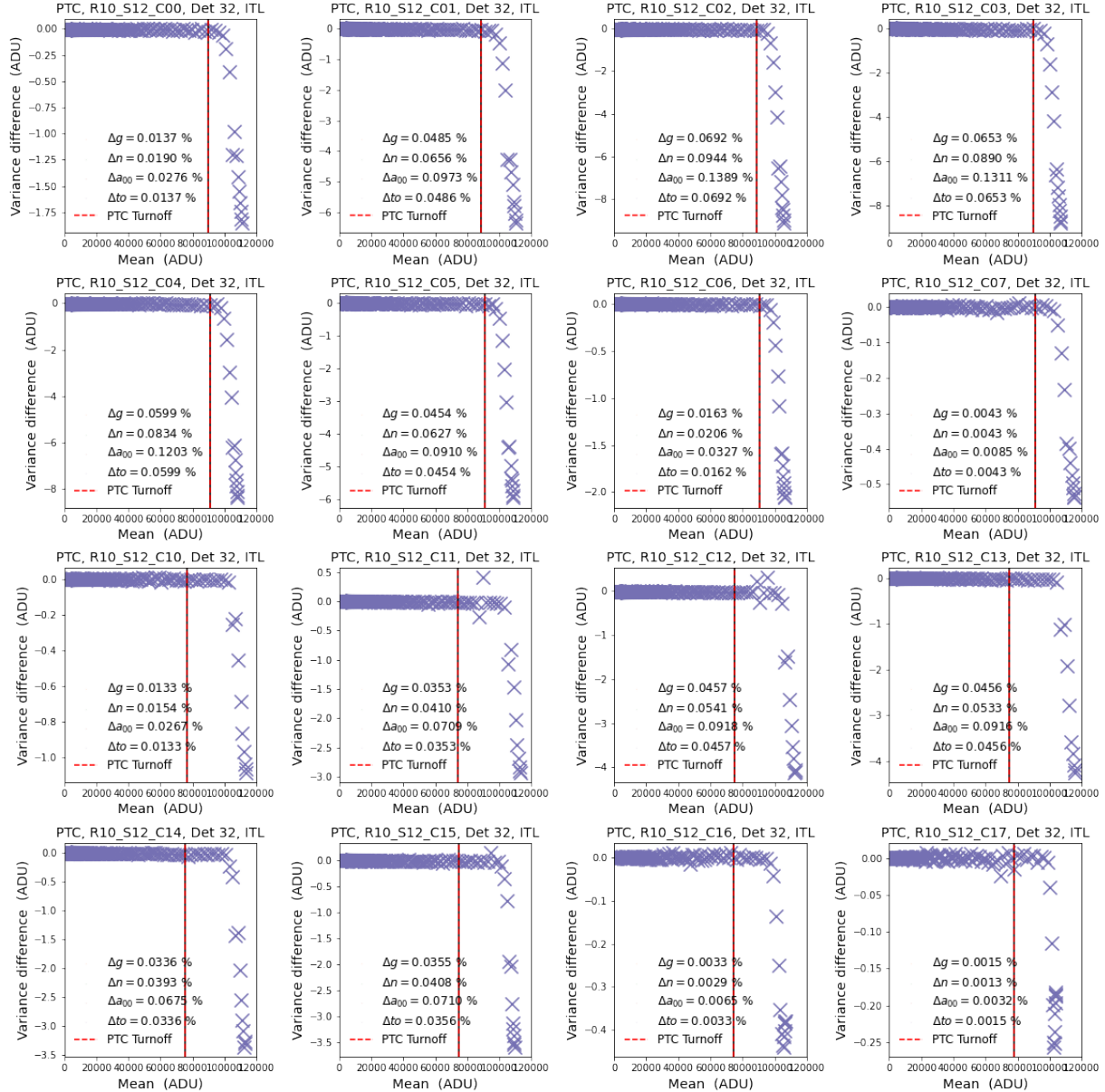


Figure 23: The plot of the variance difference vs. mean for detector 32 (R10_S12) for vendor ITL, where the variance difference is between the variance value without and with crosstalk correction. This is shown for each CCD segment, where the vertical lines mark the PTC-turnoff values. In the legends, we displayed the differences between the parameters: Δg for the gain, Δn for the read noise, Δa_{00} for the brighter-fatter effect coefficient, and Δt_0 for the PTC-turnoff.

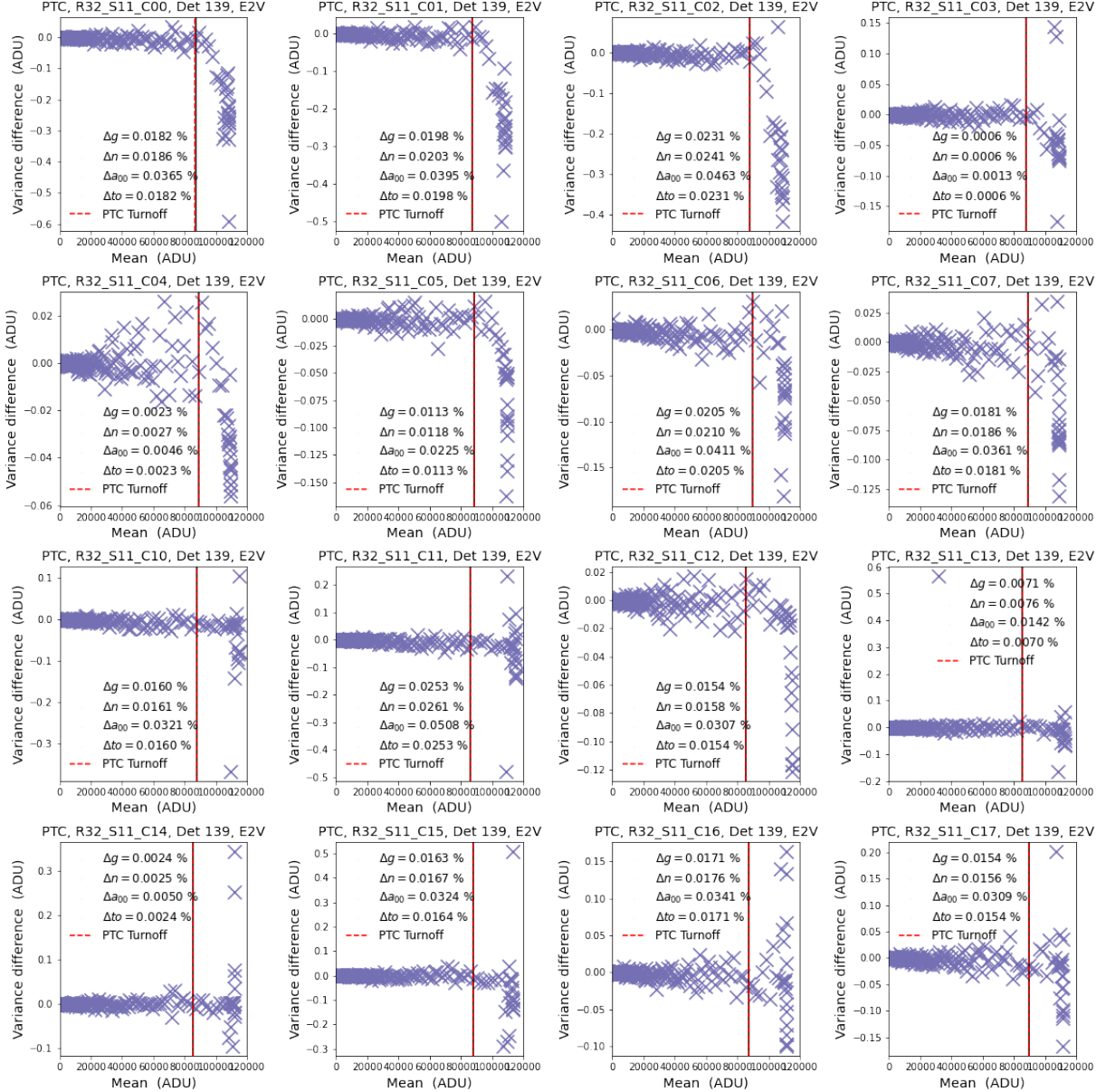


Figure 24: Refer to the description of the figure 23. This plot is for detector 139 (R32_S11) for vendor E2V.

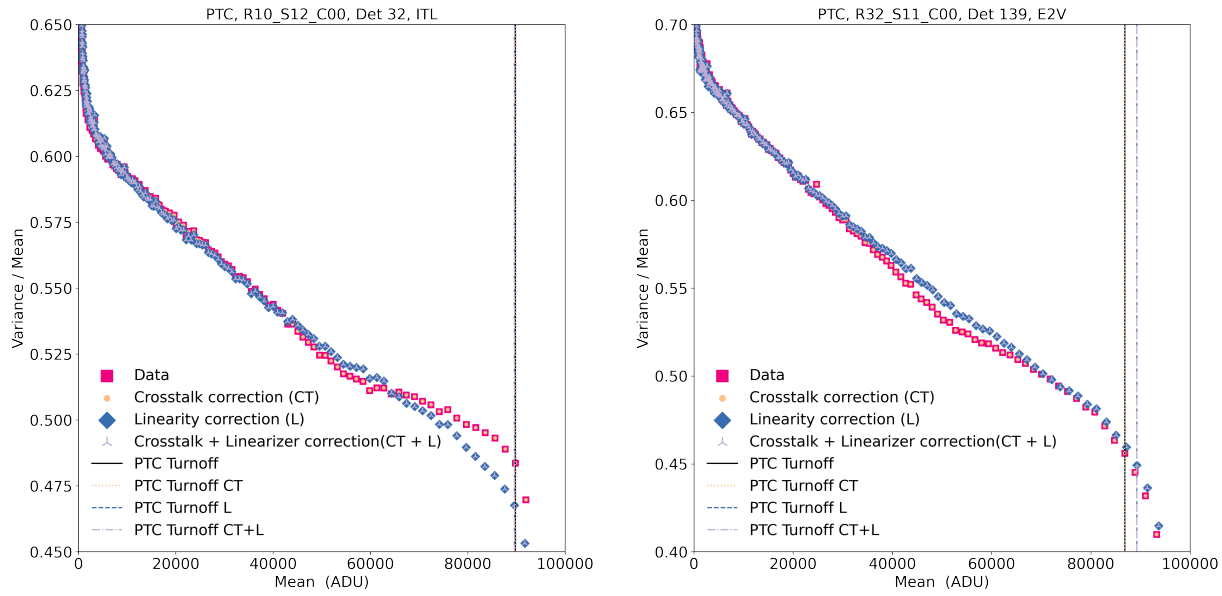


Figure 25: Variance normalized by mean vs. mean, for detector 32 (R10_S12) for vendor ITL, on the left, and for detector 139 (R32_S11) for vendor E2V, on the right. We show the data with no correction by crosstalk (CT) and nonlinearity in magenta squares. The orange dots show the data corrected for CT. The data corrected for nonlinearity with blue diamonds. Also, the triangles for data with corrections by both effects: TC and nonlinearity. Finally, the vertical lines represent the location of the turnoff.